POLITECNICO DI TORINO

Bachelor of Science

in Aerospace Engineering

Bachelor's Thesis

APPLICATION OF CFD IN THE STUDY OF SOME HEALTH DISEASES IN RESPIRATORY SYSTEM

Supervisor

Prof. Stefania Scarsoglio

Candidate

Andrea Palmarini

MARCH 2019

CONTENTS

INTRODUCTION

This work aims to illustrate the developments of the CFD (Computational Fluid Dynamics) in the comprehension and possible resolutions of some problems inherent in human health, in particular in the respiratory system. Indeed, the illnesses linked with this apparatus are various, from the simple cold to serious diseases like tumours. Hence, the scientific research has been continuing to apply new tools in order to understand and sort out these problems, such as the application of CFD which has been at the cutting edge for years.
Therefore, a mathematical background and illustration of the main developments of CFD have been reported to explain the techniques used to simplify the problem

Firstly, a brief account of the Biofluid dynamics and the respiratory apparatus has been reported in order to figure out better the parts interested by the innovative approaches and display in our mind the differences with the traditional ones, especially the inside of the nose with its cavities, muscles and membranes. Besides, a precise description of the mathematical models, such as the discretization, in CFD and its applications in biomedical systems has been set out.

In the third part of this dissertation, two recent applications of CFD have been reported: a new breath test for the detecting of the bronchial squamous tumours and the OPTINOSE® drug releasing device. These two examples are not only important for what concerns the theoretical aspects, linked with the mathematical bases behind their development, but they have also a practical relevance. Indeed, the first one is a modern and non-invasive approach in the localization of a particular kind of tumour within the respiratory apparatus by allowing to determine its severity and afterwards formulate a targeted drug delivery plan to treat the disease; whilst, OPTINOSE device lets cure more satisfactorily migraines and other headaches throughout nasal ways by employing a bidirectional release system.

CHAPTER 1

BIOFLUID DYNAMICS

Biofluid dynamics is a branch of the Fluid dynamics which deals with Biology, including pure and applied aspects. It can be distinguished in two halves: external biofluid dynamics and internal biofluid dynamics**.** The first one covers animal locomotion through surrounding fluid media (water and air), while the second one deals with heat and mass transport by fluid flow systems within an animal. They both try to understand the functioning and the evolution of those complex systems within which fluid flows work and thanks to which animals have been able to survive, evolve and generate offspring. Besides, these two halves differ from the rest of the fluid dynamics because the fluid movements are energized by the working of motile inner or outer surfaces which are flexible. Although the biofluid dynamics has a biological interest, the solutions developed by animals to some fluid dynamical problems posed by nature have been surveyed by engineers who have obtained some remarkable results by analysing them. For instance, medicine requires information from the internal biofluid dynamics of man (figure 1.1), likewise the pest control research and the veterinary and zoology research find numerous advantages from the external biofluid dynamics (figure 1.2 and 1.3). Especially the study of the respiratory system is overriding in this dissertation [1].
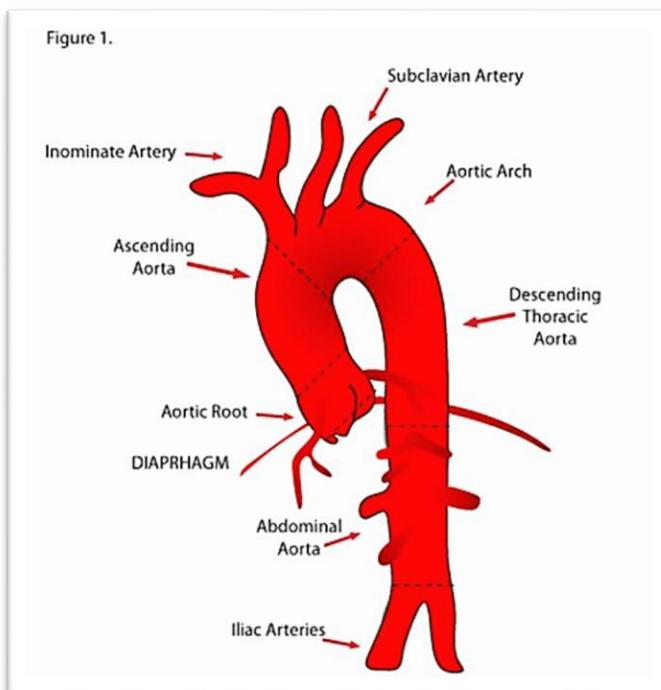
Figure 1.1 Representation of the aortic arch. When there is aortic stenosis or during an effort turbulence appears in the aorta, while in the rest of the network a laminar pattern can be applied.

Figure 1.2 Example of animal locomotion. The hydromechanics of aquatic animal propulsion is analysed by Biofluid dynamics.

Figure 1.3 Example of animal locomotion. With respect to the eel the hydrodynamical 'elongated-body theory' is very useful in the study of its movement.

CHAPTER 2

ELEMENTS OF RESPIRATORY APPARATUS

2.1 COMPOSITION

The respiratory apparatus (figure 2.1) is made up of a group of hollow organs, airways, and two parenchymatous organs: the lungs. The airways are two channels which bring the air from the outside to the lungs and they are represented by the nose, pharynx, larynx, traches and bronchi. The lungs are the organs where the exchanges between air and blood, assuring to the second one the intake of oxygen and the elimination of carbon dioxide, happen. For what concerns the anatomic and functional aspect there is a strong relation between the cardiovascular apparatus and the respiratory one [2].
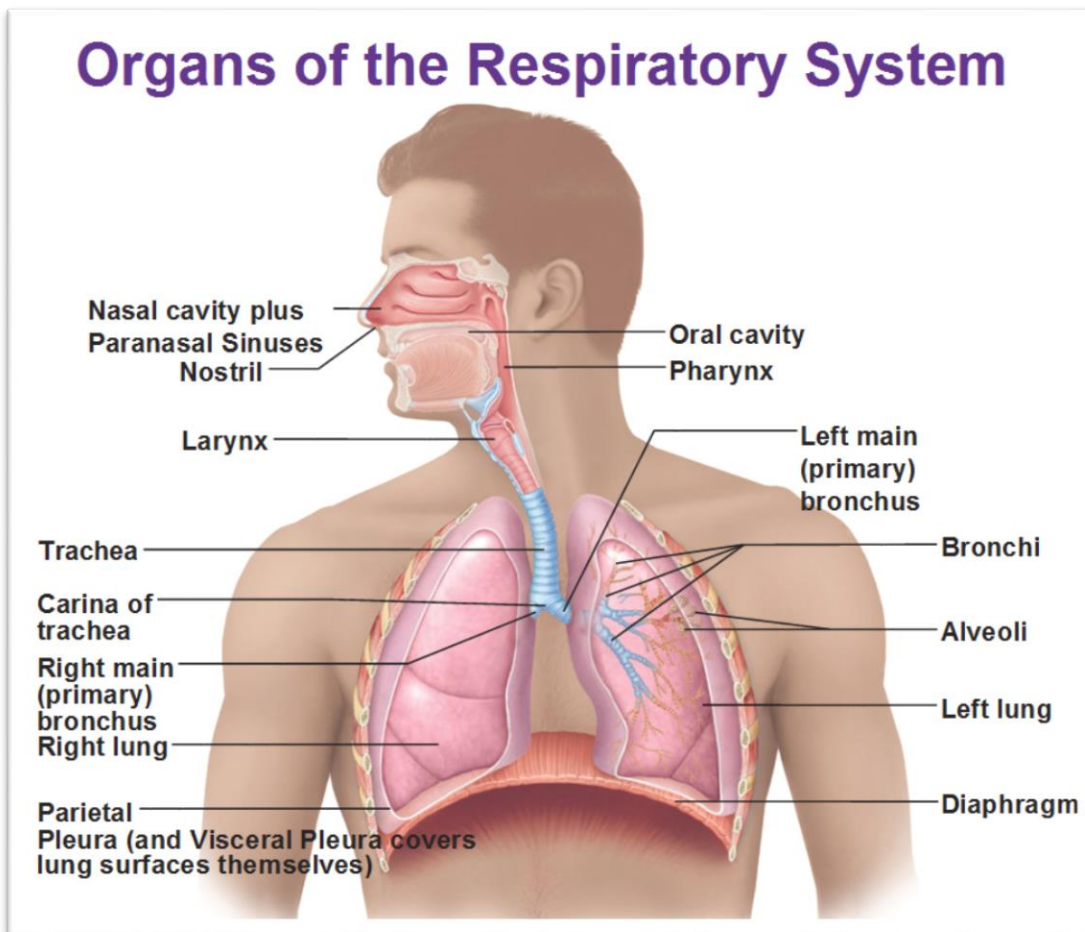

Figure 2.1 Scheme of the respiratory apparatus.

2.2 RESPIRATION

The breathing is carried out in two steps: inspiration, throughout which the air full of O_2 goes inside the lungs from the outside and through the airways; the expiration, during which the air rich of CO_2 flows contrarily towards the outside, hence within the lungs there is a gaseous exchange between the air and the blood.
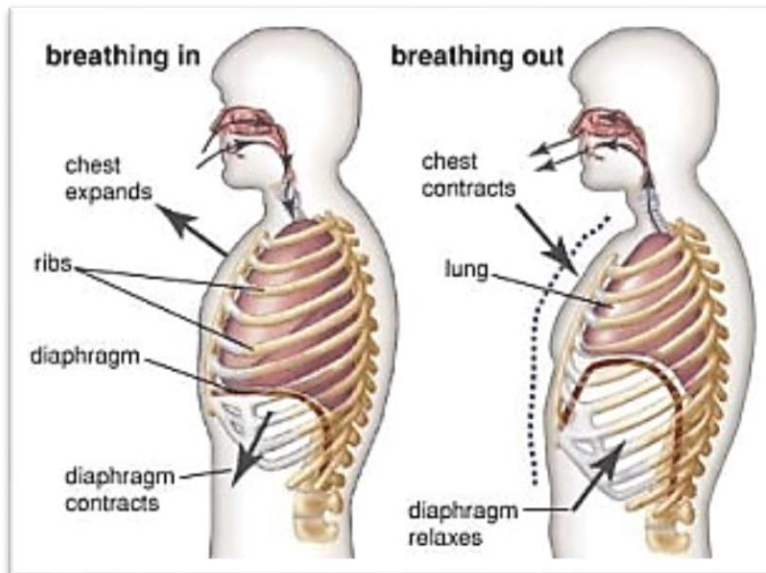
This mechanism is allowed by the diaphragm which is a muscle located between the thoracic cavity and the abdominal one. This muscle, thanks to its contraction and relaxation, allows the lungs to expand, when it gets down, and it lets them empty, when it gets up (figure 2.2.1).

Figure 2.2.1 The mechanism of breathing. It is based on the diaphragm movement.

The second breathing, called internal or cellular respiration (figure 2.2.2), consists in the use of oxygen by the cells for the combustion of nutrients, with the consequent production of carbon dioxide. It occurs in cells, particularly in mitochondria. Oxygen, present in high concentration in the blood vessels, spreads through the walls of the capillaries and penetrates into the cells, where it is used by the mitochondria for the combustion of nutrients. At the same time the carbon dioxide produced by combustion, present in high concentration in the cells, spreads through the cell membrane and passes into the capillaries: here it binds to the blood that carries it in the pulmonary alveoli [2].
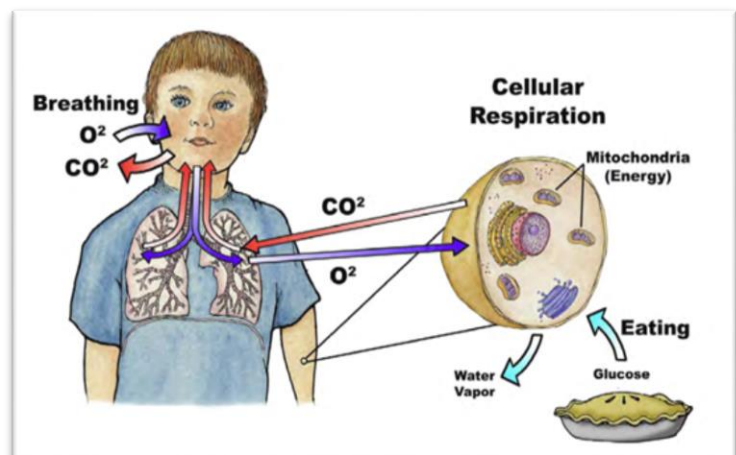

Figure 2.2.2 Cellular respiration. During this breathing O_2 and CO_2 are exchanged by diffusion.

2.3 THE ALVEOLI AND THE LUNGS

Overall the alveoli, which are concamerations within the pulmonary vesicles, present at the end of the bronchi, are more than 750 million and they have a surface of 200 m^2. The wall of the alveoli is made up of a slight membrane, over which a dense network of capillaries spreads (figure 2.3.1). The set of all the alveoli forms two elastic spongy masses that occupy the thoracic cavity and are called lungs
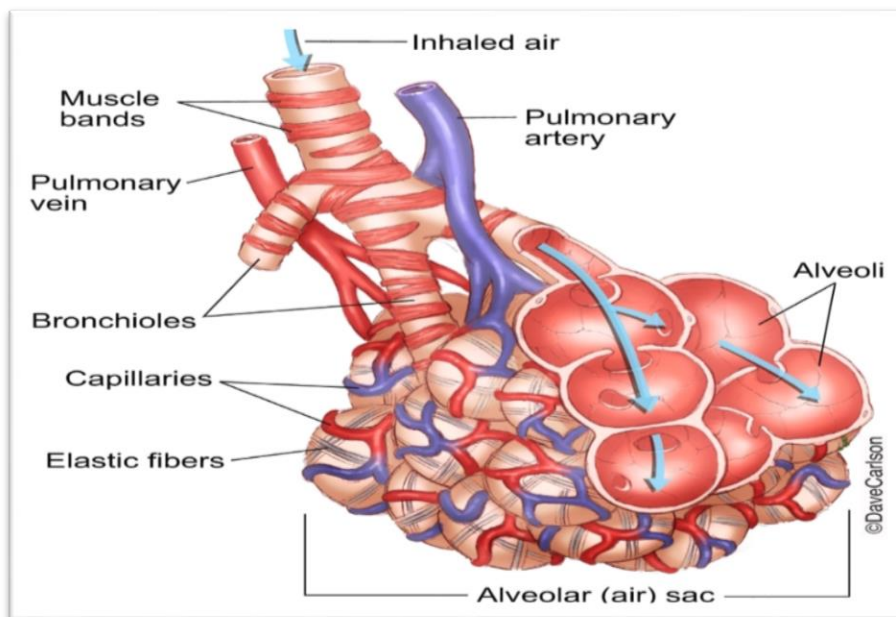
Figure 2.3.1 The structure of alveoli. They are covered by capillaries throughout which the exchange between O_2 and CO_2 happens.

The lungs are wrapped by a double wall serous membrane, namely the pleura (figure 2.3.2), and between these two walls there is a fine veil of liquid which allows the scroll of the two layers on each other in order to reduce the friction between the lung's surface and the ribs during the respiration. Moreover, each lung receives the venous blood from the pulmonary artery and it gives the first one purified back to the heart trough pulmonary veins [2].
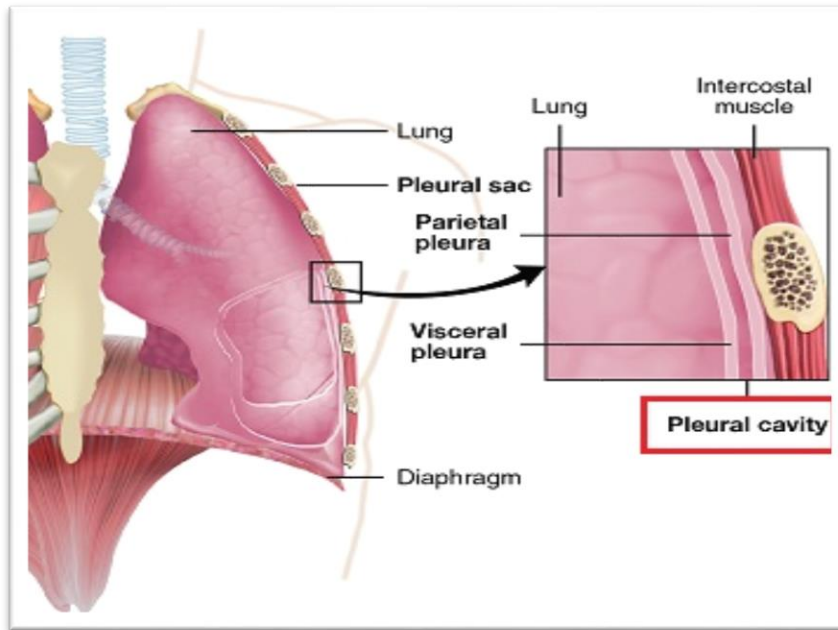
Figure 2.3.2 The coating of the lungs. Pleura allows to reduce the friction between the lung and ribs during the breathing.

2.4 THE NOSE AND NASAL CAVITIES

The nose is characterized by two nasal passages, divided by the nasal septum, and they open independently into the upper part of the throat, namely the nasopharynx. The lateral walls, which form the external nose, have ridges formed of the turbinate bones. The inferior, middle and superior meatus are situated below and sideways to the turbinates (figure 2.4.1). The paranasal sinuses are hollow air-filled spaces which open into the nasal passages. The maxillary, frontal and ethmoid sinuses lead into the middle meatus, while the sphenoid sinuses open in the back of the nasal cavities. The olfactory mucosa (or olfactory cleft) is located in the roof of the nasal cavity and almost 2-3 cm from the nostrils there is the triangular shaped nasal valve (figure 2.4.2). This valve fulfils in limiting dynamic flow with important influences on flow regulation and filtering capability. In the anterior area, the nasal passage is covered by non-ciliated epithelium, which progressively turns into ciliated respiratory one. In the posterior nasal cavity, the total cross-sectional area grows to let heat and moisture pass, here, the airflow enters, after the latter has gone through the triangular shaped valve region where larger particles are trapped and which is the most cramped area of the nose [2].
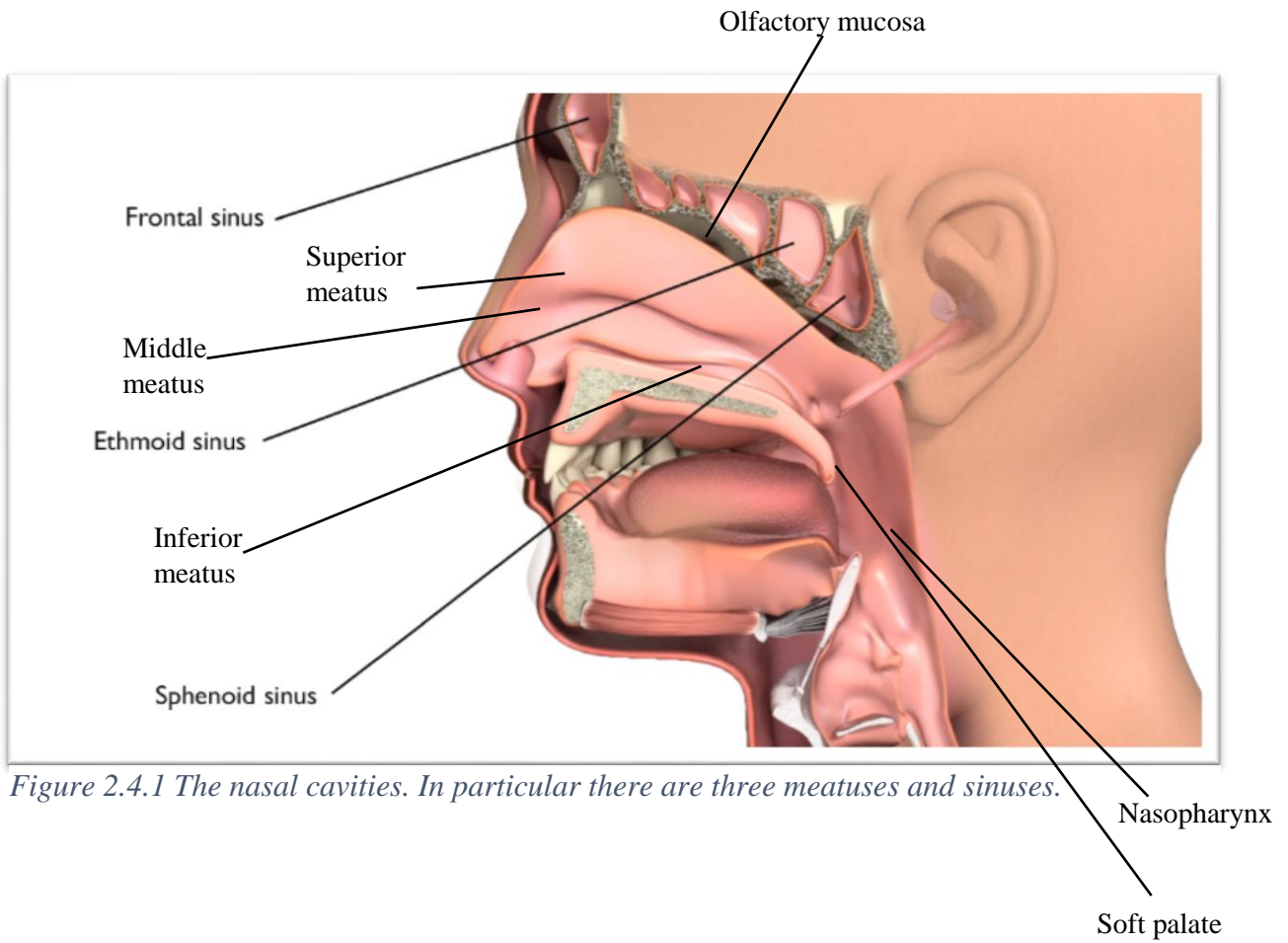
Figure 2.4.1 The nasal cavities. In particular there are three meatuses and sinuses.
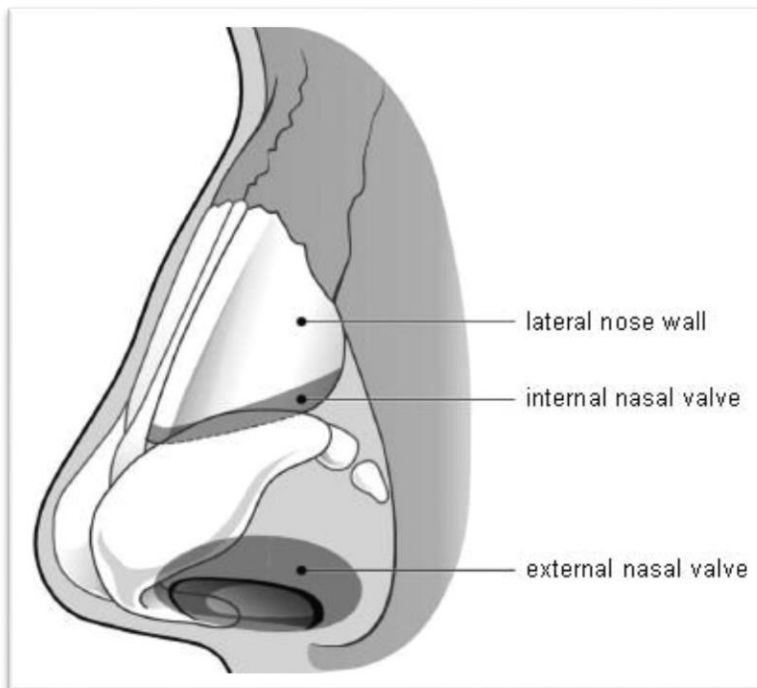

Figure 2.4.2 Nasal valves

CHAPTER 3

RESPIRATORY FLUID DYNAMICS AND FLOW PATTERNS

3.1 FLUID IN MOTION

When a fluid is in static conditions, each its particle is still with no velocity or acceleration because the resultant force between the volume forces and surface ones is null. In fact, for instance, if we consider a volume force acting on a portion of fluid, it causes a pressure variation in the directions along which the volume force operates and this pressure modification keeps the resultant force null. This behaviour is described by (3.1).

$$\nabla p = \rho \vec{f} \quad (3.1)$$

Where p is the hydrostatic pressure, ρ is fluid density and $\vec{f}$ is the unit-volume force. Moreover, this balance condition is the same either for nonideal flows and for ideal ones, namely incompressible and without viscosity ($\mu=0$) [3]. The latter is responsible of the internal friction forces opposing to the sliding between two portions of fluid and they act when a real fluid moves. These unit-surface friction forces form the tensor $\boldsymbol{\tau}$ and they are called viscous or shear stresses. Actually, either normal and shear stresses operate on a fluid in motion and they are the elements of a tensor $\boldsymbol{\Pi}$, stresses tensor, which is symmetric and it has got only six independent elements. Moreover, $\boldsymbol{\Pi}$ is defined in each point of the domain and in each time instant, so it represents a tensorial camp which is function of time and space (figure 3.1)

$$\boldsymbol{\Pi} = \begin{pmatrix} \sigma_{11} & \sigma_{12} & \sigma_{13} \\ \sigma_{21} & \sigma_{22} & \sigma_{23} \\ \sigma_{31} & \sigma_{32} & \sigma_{33} \end{pmatrix} \quad (3.2)$$
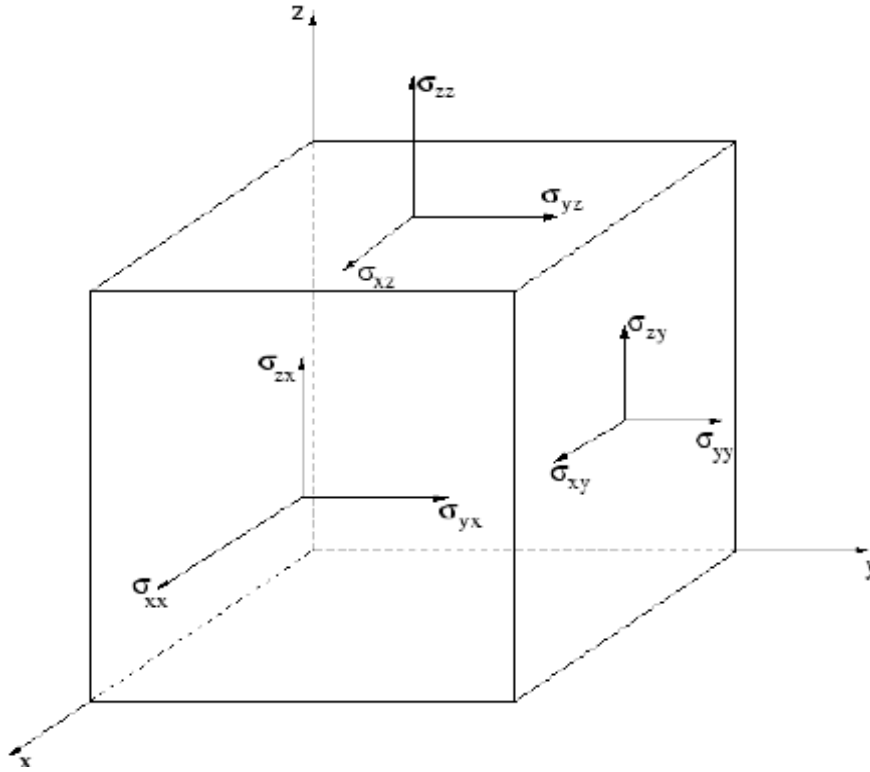
Figure 3.1 The nine components of the tensor Π: x, y and z indicate respectively 1, 2 and 3. We can note three normal components and six tangential components.

Within (3.2) we have to specify an isotropic part and a non-isotropic one, where the first one is the average value of the normal components of the stresses σ_{ij}, namely:

$$p = -\frac{1}{3}(\sigma_{11} + \sigma_{22} + \sigma_{33}) \ -\frac{1}{3}\sum_i \sigma_{ii}$$

where p is the hydrostatic pressure, while the non-isotropic part is **τ.** Thereby, we can write the full equation:

$$\Pi = -\text{p}\mathbf{I} + \boldsymbol{\tau}$$

$$\begin{pmatrix} \sigma_{11} & \sigma_{12} & \sigma_{13} \\ \sigma_{21} & \sigma_{22} & \sigma_{23} \\ \sigma_{31} & \sigma_{32} & \sigma_{33} \end{pmatrix} = \begin{pmatrix} -p & 0 & 0 \\ 0 & -p & 0 \\ 0 & 0 & -p \end{pmatrix} + \begin{pmatrix} \tau_{11} & \tau_{12} & \tau_{13} \\ \tau_{21} & \tau_{22} & \tau_{23} \\ \tau_{31} & \tau_{32} & \tau_{33} \end{pmatrix}$$

Since either **Π** and the isotropic part are symmetric, hence even **τ** has the same characteristic, its track is null and the non-diagonal elements are matched with shear stresses. The deformation of the fluid, namely its volumetric dilation ($\nabla \cdot \boldsymbol{V}$) and its shape distortion described by the non-diagonal terms of the tensor **D**, is linked with **τ:**

$$\boldsymbol{\tau} = 2\mu\mathbf{D} + \lambda(\nabla \cdot \boldsymbol{V})\mathbf{I} \quad (3.3)$$

Where μ is the viscosity coefficient, λ is applied when the fluid is compressible, **D** is the tensor of the deformation velocity with three velocity components (u,v,w) in the three space directions (x,y,z) and **I** is the identity tensor [4].

$$\boldsymbol{D} = \begin{pmatrix} \dfrac{\partial u}{\partial x} & \dfrac{1}{2}\left(\dfrac{\partial u}{\partial y}+\dfrac{\partial v}{\partial x}\right) & \dfrac{1}{2}\left(\dfrac{\partial u}{\partial z}+\dfrac{\partial w}{\partial x}\right) \\[2ex] \dfrac{1}{2}\left(\dfrac{\partial v}{\partial x}+\dfrac{\partial u}{\partial y}\right) & \dfrac{\partial v}{\partial y} & \dfrac{1}{2}\left(\dfrac{\partial v}{\partial z}+\dfrac{\partial w}{\partial y}\right) \\[2ex] \dfrac{1}{2}\left(\dfrac{\partial w}{\partial x}+\dfrac{\partial u}{\partial z}\right) & \dfrac{1}{2}\left(\dfrac{\partial w}{\partial y}+\dfrac{\partial v}{\partial z}\right) & \dfrac{\partial w}{\partial z} \end{pmatrix}$$

(3.3) in cartesian components becomes:

$$\tau_{ij} = \mu\left(\frac{\partial u_i}{\partial x_j}+\frac{\partial u_j}{\partial x_i}\right) + \lambda\delta_{ij}\frac{\partial u_k}{\partial x_k} \quad (3.4)$$

Where δ_{ij} is Kronecker delta which is an order two tensor and it values 1 if i=j and 0 if i≠j

3.2 ENERGY DISSIPATION AND BOUNDARY LAYER

In a viscous fluid in motion, such as air, it is possible to calculate the unit-mass energy dissipation (3.4) as of the velocity, either for flows disturbed by one bifurcation or by two in series.

$$\Phi = \frac{1}{\rho}(\boldsymbol{\tau}\cdot\nabla)\cdot\vec{V} \quad (3.5)$$

Where ρ is the density, $\boldsymbol{\tau}$ is the viscous stress tensor and $\vec{V}$ is the velocity vector. (3.4) points out the dissipation of mechanical energy caused by viscosity and its transformation in internal energy. The dissipation of energy is concentrated in a boundary layer which, over a tube like the airways, results from that of the flat plate by imagining to wrap it on herself and it includes the zone with the peak of the velocity and the pipe wall. Indeed, the boundary layer is a region, within the fluid in contact to a solid surface, where the velocity changes from zero on the wall to the value of the speed of the undisturbed fluid. The dimension of this zone depends on the Reynolds number (Re) which compares the inertial stresses with the viscous ones:

$$Re = \frac{U_\infty L}{\nu}$$

In particular this region of the connection between the velocity on the wall and U_∞ (the speed of the undisturbed stream which wets the plate) is determined by the viscous stresses, in fact they speed up the slowest fluid portions and slow down those which are faster in order to uniform the velocity profiles. In particular in our case of a flat plate, which is considered in two dimensions (x,z), (3.3) is more simply, in fact we can write, if the fluid is incompressible and with only the component u(x,z) of the velocity:

$$\tau = \mu\frac{\partial u}{\partial z}$$

We can consider the viscosity prominent within the boundary layer, but it can be neglected outside because there are not velocity gradients causing viscous stresses, moreover this junction zone between the two velocities decreases in dimension with the growth of Reynolds number.

We can define a thickness $\delta(x)$, whose growth along the plate is linked with the dependence of u on x, and it is defined as the value of z thanks to which $u = 0.99U_\infty$, namely the speed inside the boundary layer (u) has the same value of that outside. Besides the flow in this zone can be laminar or turbulent according to the Re, if it is laminar ($Re < 5 \cdot 10^5$) the fluid particles flow neatly along parallel streamlines and adjacent, this kind of motion characterizes the airways and it is unstable depending on velocity, whilst if the motion is turbulent, there are swirling structures, eddies and the particles move messily by not following a certain pattern. They carry out fluctuations highly dissipative which cause a remarkable flattening of the average velocity profiles (u), furthermore this motion, in which the inertial forces rule over the viscous ones, needs much energy. For the laminar regime δ is:

$$\delta = 5\sqrt{\frac{vx}{U_\infty}} \approx \sqrt{x}$$

Instead in the turbulent one:

$$\delta = 0.37x\left(\frac{U_\infty x}{v}\right)^{-1/5} \approx x^{4/5}$$

Therefore, in this last case thickness increases mostly. Likewise, with respect to the drag coefficient (C_D), we can note a noticeable growth in the drag due to the loss of momentum of the air molecules because of mixing and consequent heating, in fact while in the linear regime:

$$C_D = \frac{1.328}{\sqrt{\frac{U_\infty L}{v}}}$$

where L is the length of the plate, in the turbulent regime:

$$C_D = \frac{0.072}{\sqrt[5]{\frac{U_\infty L}{v}}} - \frac{A}{U_\infty L / v}$$

where A is a coefficient that is 1050, 1700, 3300, 8700 respectively to Re_{cr} $3 \cdot 10^5$, $5 \cdot 10^5$, 10^6, $3 \cdot 10^6$. Re_{cr} denotes the transition point (x_{tr}) which locates the zone where laminar boundary layer becomes turbulent, for a flat plate is:

$$x_{tr} = \frac{L(5 \cdot 10^5)}{Re}$$

Besides we can note the presence of the laminar substrate, namely a slight region where the velocity reaches the zero value on the wall and the turbulent motion is fairly reduced (figure 3.2) [5].
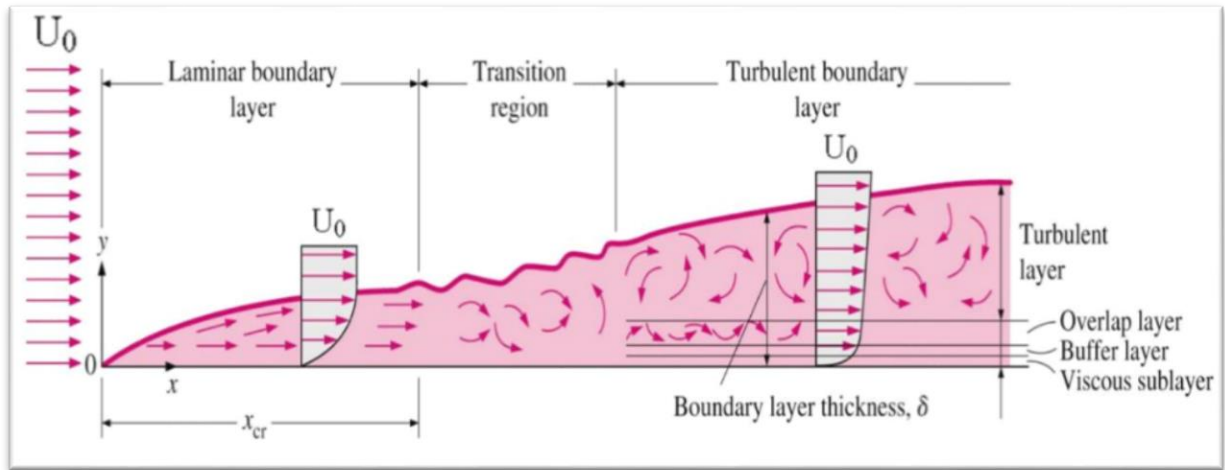
Figure 3.2 The evolution of the boundary layer. The development is determined by Reynolds number from the laminar regime, characterized by fluid portions which flow neatly, to the turbulent regime where there are some curved lines that indicate eddies.

3.3 RESPIRATORY PATTERNS

After we have discussed about the features of a general fluid in motion, it is necessary to focus on airflow patterns which develop within the human airways. Respiratory flow patterns are characterized by high Reynolds numbers and by the transport of oxygen and carbon dioxide by convection. In order to simplify the argument and understand it better, a structure constituted by one bifurcation and a parent tube has been analysed and it is shown in figure 3.3.1.
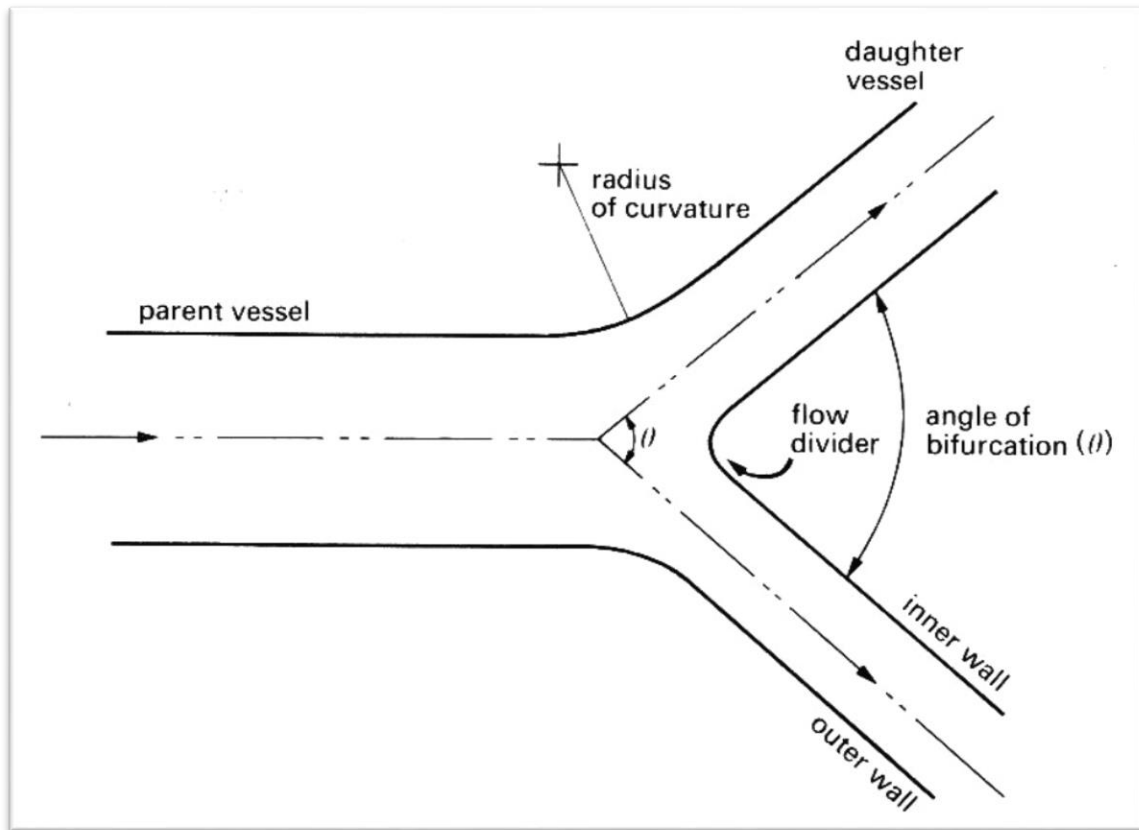
Figure 3.3.1 The bifurcation of the bronchi. We can note the parent tube splits in two daughter vessels with a certain angle of bifurcation, besides each tube present an inner and an outer wall. Figure taken from Hong Liu, Peiwen L., Even distribution/dividing of single-phase fluids by symmetric bifurcation of flow channels, International Journal of Heat and Fluid Flow Volume 40, April 2013, Pages 165-179.

The ratio of the tube length to an earlier tube diameter is prominent and it is usually not high, so that just a scarce distance allows the velocity distribution, which had already been distressed by a previous bifurcation, to slow down before being again disturbed. Furthermore, the distribution of the velocity within airways is dissimilar from that of Poiseuille, which is easier to study and it presents a mass flow rate in a straight tube (figure 3.3.2):

$$Q = \frac{-\pi R^4}{8\mu} \frac{dp}{dz}$$

Where:

$\frac{dp}{dz}$ is the pressure gradient between the two ends

μ is the dynamic viscosity,

Q is the mass flow rate,

R is the pipe radius.

Figure 3.3.2 The mass flow rate of the Poiseuille flows in a pipe.

Indeed, we could not apply this simplification, because Hagen-Poiseuille law is verified only when the pipe radius, namely in our case the airways, is very small, instead for greater ra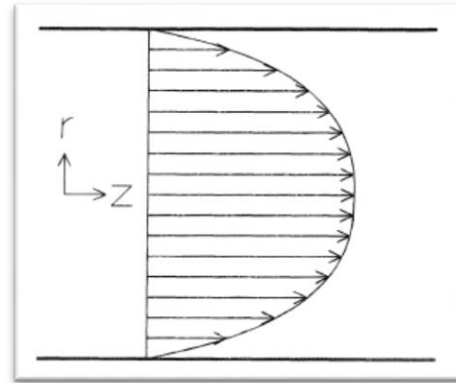diuses there is a critical value of the speed beyond which eddies appear in the flow: turbulent flow. The mechanisms which cause the development of the eddies are linked with noticeable velocity variations orthogonally to the streamlines and with the high viscous forces if the fluid is real, like air. Other determinant elements are the presence of obstacles and shape variations in the means which appear in the airways [3]. Thereby, in order to adapt the distribution of velocity to that of Poiseuille, it needs an entry region which is an area, following the entrance of the pipe, long about:

$$(0.03 \cdot Re)d \quad (3.6)$$

where Re is the Reynolds number based on the diameter d and the initial speed U_0 (figure 3.3.3) [1]. In this zone the effects originating from the interior wall of the pipe propagate into the flow as an expanding boundary layer. When the boundary layer expands to fill the entire airway, the developing flow becomes a fully developed one, where its characteristics no longer change with increased distance along the airway. The fluid enters at a uniform velocity, however due to viscous forces within the fluid, the layer in contact with the pipe surface resists the motion of adjacent layers and slows them down gradually by forming a velocity profile. For the mass conservation (3.7), the velocity of layers of the fluid in the middle of the pipe increases to compensate for the reduced velocities of the layers of fluid near the pipe surface. This develops a velocity gradient across the cross section of the pipe and the velocity distribution comes within 5% of a Poiseuille one.

$$\frac{\partial \rho}{\partial t} + \nabla \cdot (\rho \mathbf{V}) = 0 \quad (3.7)$$
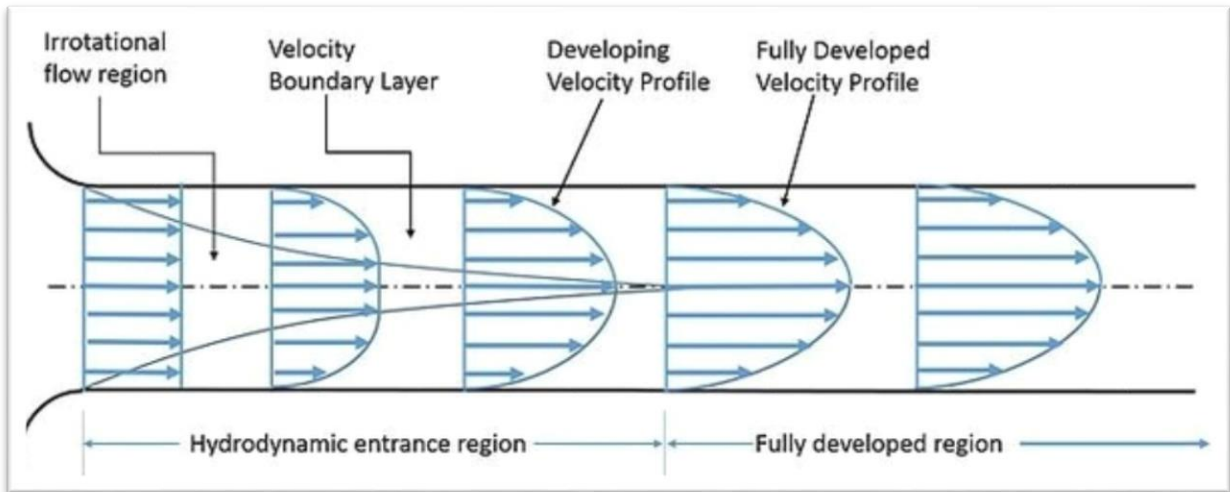
Figure 3.3.3 The hydrodynamic entry region. It depends on the diameter of the pipe and thanks to which the fluid adapts to the tube until reaching a full developed velocity profile.

Nevertheless, in our case described by figure (3.3.1) a greater entry region (3.6) is required to adapt the distribution of velocity to that of Poiseuille, in fact, if earlier the departure from the second one was just 5%, now we can find a deeper difference, since on the right hand there is a thin boundary layer on the flow divider, where the velocity outside the latter is similar to that in the parent tube, and on the left hand the secondary flows, originated by the curved motion in the bifurcation, increase like the peak of the velocity reached on the outside bend by the curved motion [1]. Indeed, airways are not always straight and they display bends, namely the bifurcations due to which the airflow is curved and the centrifuge force originating (3.8) generates secondary flows.

$$\vec{F} = m\omega^2 \frac{d}{2} \ (3.8)$$

Where d is the diameter and ω is the angular speed. This force produces a secondary flow with the movement of central fluid towards the outside bend and a return one towards the inside curve near the wall, besides this effect is quite well seen at high Reynolds. The flow, under the action of a steady pressure gradient, is accelerated towards the outside bend of the central fluid, whilst the return flow decelerated by the viscosity is confined to a thin boundary layer (figure 3.3.4).
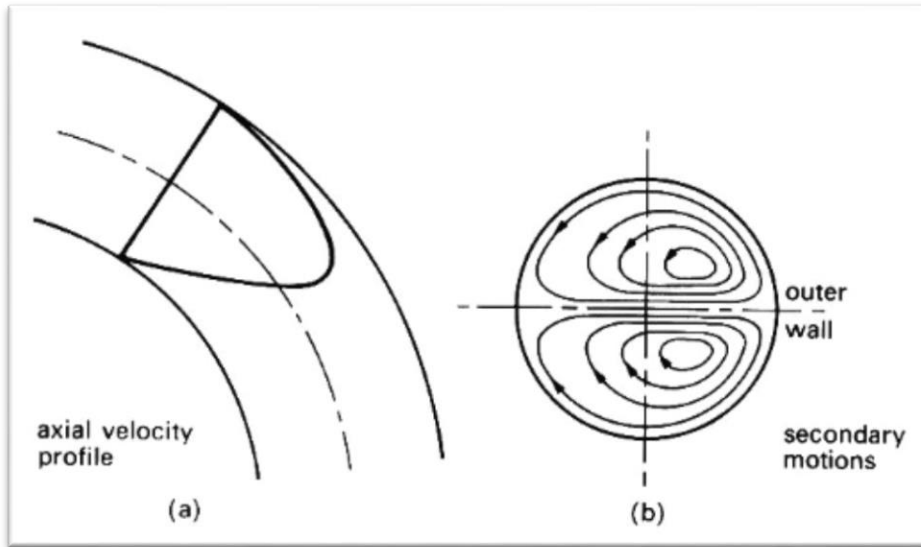
Figure 3.3.4 (a) Distortion of the axial velocity profile as a result of tube curvature, (b) Projection of streamlines on a transverse plane, clearly showing the form of the secondary motion. Figure taken from Caro C.G., Pedley T.J., Schroter R.C., Seed W.A.,1978, The Mechanics of the Circulation, Oxford University Press.

We can also note a major presence of shear-rates along the outside of the bend, these stresses lead to a higher dissipation of mechanical energy (3.5) by viscosity and deformation of the fluid elements ($\nabla \cdot V$). These aspects mean a significative increase of pressure gradient to keep a constant volume flow rate through a curved pipe rather than through a straight one [6].

With respect to the boundary layer of the airflow, we know that energy dissipation (3.5) is concentrated above all in the boundary layer. In this region velocity gradients are of order U_∞/δ and energy dissipation of order $\mu(U_\infty/\delta)^2$ per unit volume, while for unit-length tube μU^2_∞ (d/δ). If we make a ratio between this energy dissipation and that of Poiseuille flow and we consider the length L as a multiple of the diameter d, we obtain:

$$0.33 \left(\frac{Re \cdot d}{L}\right)^{1/2} \quad (3.9)$$

(3.9) is sensitive mainly to the Reynolds number based on diameter and on speed, the reason of this dependence can be found in a fluid which has got its velocity peak very close to the wall of the tube that is showed in the figure 3.3.5 from Pedley, Schroter and Sudlow's survey [7]. In fact, we can see three different velocity profiles in three distinct diameters in a daughter vessel downstream of the bifurcation for a Reynolds number of 700 (a) and the Poiseuille distribution in the related parent vessel (b). It is fairly remarkable nearby the flow divider some peaks of the velocity profiles which are preserved along the whole daughter vessel. Furthermore, we can identify some particular Reynolds numbers whenever there is light or heavy breathing, in the first case (30L/minute) Re varies from 2325 in the trachea to 369 in the fifth-generation airways

and 32 in the tenth one, while in the second case (120L/minute) we have to quadruple the previous values (figure 3.3.6).
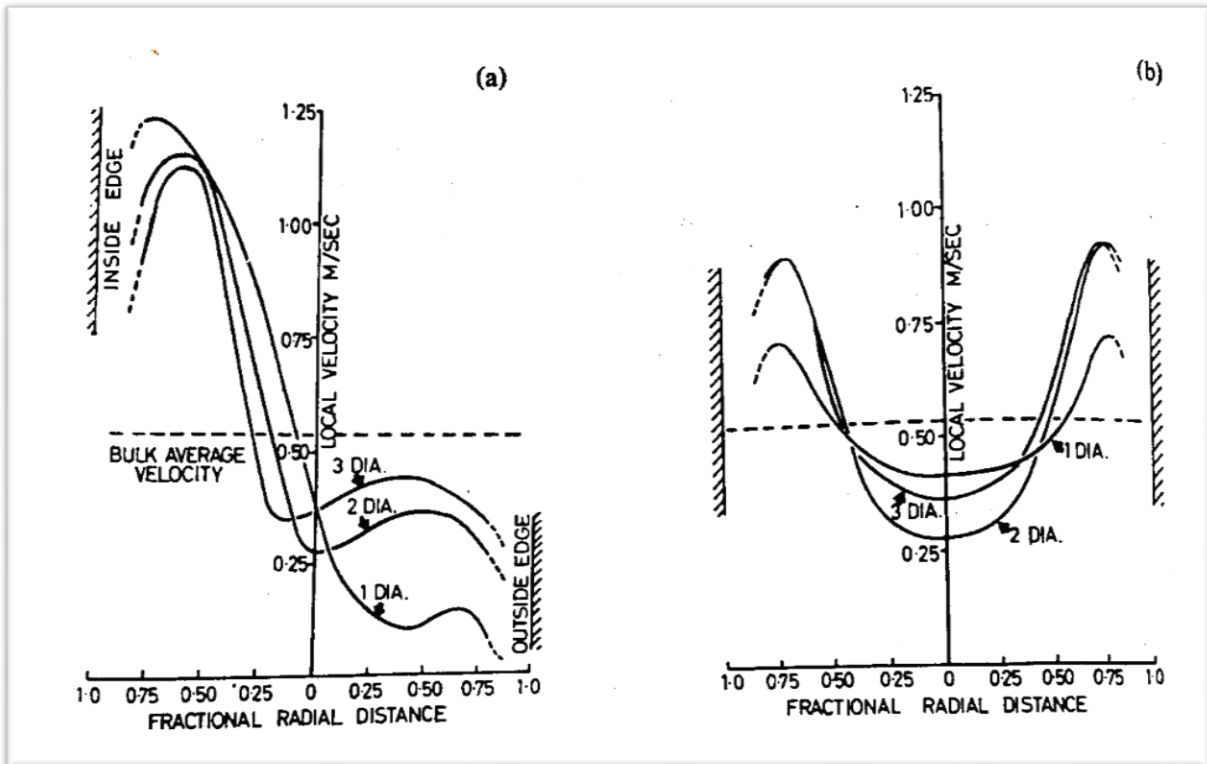

Figure 3.3.5   The behaviour of a fluid of Re 700 which runs throughout three different diameters in a daughter vessel (a) and in the parent tube (b). Figure taken from Pedley T. J., Schroter R. C., Sudlow M. F., 1970, Respiration physiology, 9, 371-405.

TABLE 2.3

Human Airway Dimensions, Velocities, and Reynolds Numbers

Generation	Internal diameter (cm)	Length (cm)	Quiet breathing ($Q = 0.5 \times 10^{-3}$ m^3 s^{-1})		Vigorous breathing ($Q = 2.0 \times 10^{-3}$ m^3 s^{-1})	
			$\bar{v}$ (cm s^{-1})	Re	$\bar{v}$ (cm s^{-1})	Re
Trachea	1.80	12.0	197	2,325	790	9,324
1	1.22	4.76	215	1,719	859	6,876
2	0.83	1.90	235	1,281	941	5,124
3	0.56	0.76	250	921	1,002	3,684
4	0.45	1.27	202	594	809	2,376
5	0.35	1.07	161	369	643	1,476
10	0.13	0.46	38	32	151	127
15	0.066	0.20	4.4	1.9	17.8	7.6
20	0.045	0.083	0.3	0.09	1.2	0.37

Source: Reproduced from Ref. [18], with permission of www.annualreviews.org © 1977.

Figure 3.3.6 The Reynolds possible values for quiet and vigorous breathing by setting off from trachea to twentieth generation of branches. Figure taken from Reproduced from Ref. [18, with permission of www.annualreviews.org], 1977.

The first generations of lung airways are able to reduce gradually total pressure (3.10) in inspiratory flow

$$H = p + \rho g z + \frac{1}{2}\rho U_\infty{}^2 \quad (3.10)$$

and they make loss of total pressure (3.11) proportional to $(U_\infty)^{3/2}$:

$$\Delta H = \frac{fLU_\infty{}^2}{2D} \quad (3.11)$$

Where D is hydraulic diameter and f is the friction coefficient depending on Re=Ud/v, namely on viscous action. In the case of turbulent flow (Re>4000):

$$f = \frac{0.32}{Re^{0.25}} \quad (3.12)$$

hence by putting (3.12) in (3.11), we obtain $\Delta H \; \alpha \; (U_\infty)^{7/4}$ (3.13). We can also define (3.11) like energy loss per unit mass by knowing f:

$$\phi = E_K \cdot f$$

Where E_K is the kinetic energy, thereby in turbulent motion:

$$\phi = \frac{1}{2}\frac{0.32 U_\infty{}^2}{Re^{0.25}} \approx U_\infty{}^{7/4} \quad (3.14)$$

Actually, from figure 3.3.6 it is clear that the turbulence has already appeared since the flow runs along the first generations of lung airways during heavy respiration, however a new viscous boundary layer creates over the flow divider within which (3.13) is preserved although the presence of turbulence motion. Figure 3.3.7, from [7], shows the drop of total pressure, called 'viscous pressure' due to viscous force, either for real fluid and for Poiseuille's one

through generations of lung airways during quiet breathing (10L/minute), figure 3.3.7 (a), and vigorous breathing (100L/minute), figure 3.3.7 (b), by assuming that (3.9) is preserved.
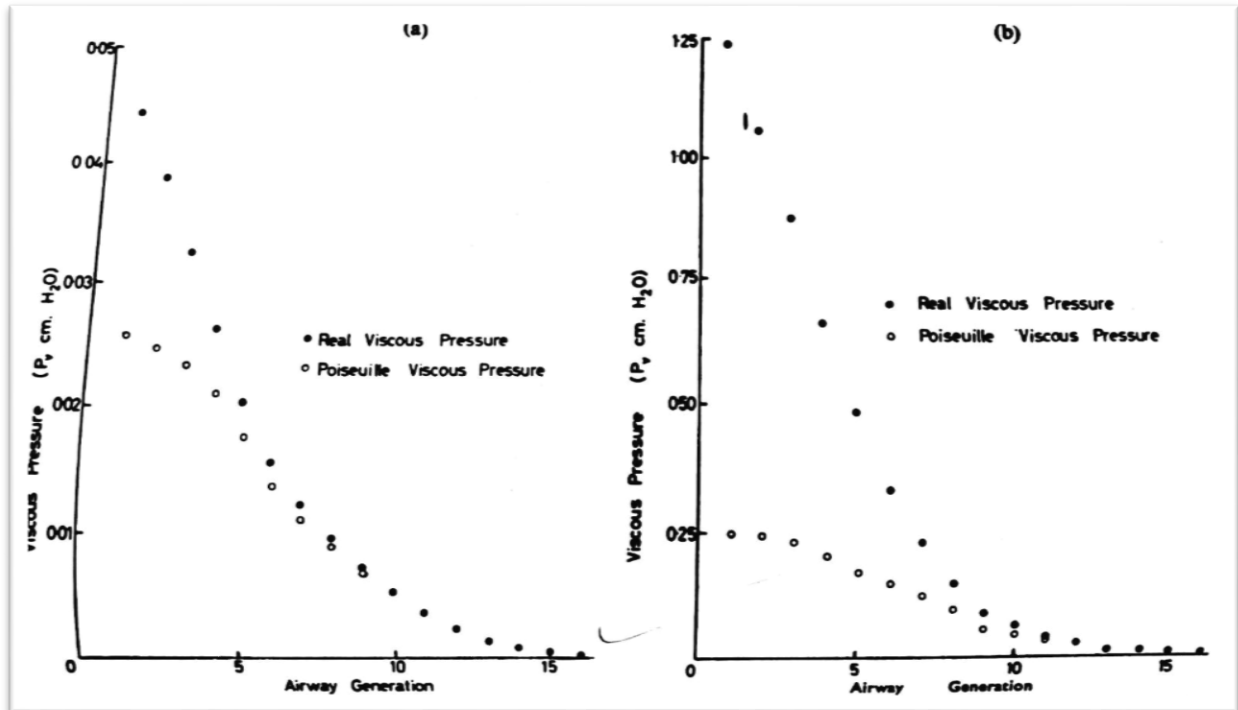

Figure 3.3.7 The trend of total pressure drop during light and heavy breathing. It is remarkable that the difference between the real and Poiseuille's flow has already been evident during light respiration and much more manifest during heavy breathing. Figure taken from Pedley T. J., Schroter R. C., Sudlow M. F., 1970, Respiration physiology, 9, 371-405.

3.4 PROBLEMS WITH THE ANALYSIS OF FLOWS WITHIN THE HUMAN BODY

In accordance with what has been reported, we can maintain that there are some disadvantages in the account of the flows within the human body which makes the analysis difficult [1]:

- A certain complexity of tube branches: the respiratory system is extremely branched because it is characterized by a dense network of tubes. Indeed, the air entering the trachea is subdivided after some separate branches in many hundreds of million small flows in the zone of the alveoli.
- Unusual range of Reynolds number: in the airways the Reynolds number can assume values from a few hundred for up to ten thousand, according to figure 3.3.6. Moreover, airflows are more complex than Poiseuille's flow, since the centrifugal force (3.8), originating in bronchioles, causes secondary flows and due to the presence of the enormously long entry region (3.6) which is necessary to make the flow like that of Poiseuille in a straight tube.
- A strong elasticity: the vessels containing airflow present a complicated capability of distension.
- Particular fluid properties: there is not a constant viscosity μ due to the presence of dust particles in suspension in the airflow.

CHAPTER 4

FUNDAMENTALS OF COMPUTATIONAL FLUID DYNAMICS

The CFD allows to sort out the equations of the fluid motion and geometry by employing some numerical techniques and the discretization, which refers to the process of converting or partitioning continuous attributes, features or variables to discretized or nominal attributes, features, variables, intervals. Among these procedures there are: the finite volume method, the finite element method and multifractal analysis. These techniques are explained briefly and simply below, because they are the mathematical base of results achieved in the two examples reported in the following chapters.

4.1 THE FINITE VOLUME METHOD

This method is used to represent and estimate partial differential equations in the form of algebraic equations. Values are calculated at discrete places on a meshed geometry. "Finite volume" refers to the small volume surrounding each node point on a mesh. In this method, volume integrals in a partial differential equation, which contains a divergence term, are converted to surface integrals:

$$\oiint f dS = \iint f(\boldsymbol{r}\,(u,v)||\boldsymbol{N}(u,v)||dudv$$

by using the divergence theorem:

$$\iiint_V (\boldsymbol{\nabla} \cdot \mathbf{F})\, dV = \oiint_S \mathbf{F} \cdot d\mathbf{S}$$

These terms are then evaluated as fluxes at the surfaces of each finite volume. Because the flux entering a given volume is identical to that leaving the adjacent volume, these methods are conservative.
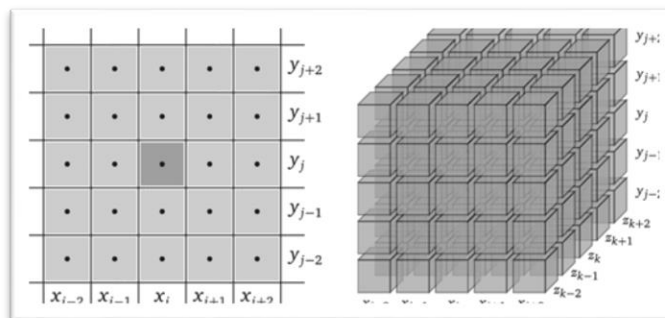

Figure 4.1 A cell in R³ with finite volume method. Figure taken from F. Moukalled L. Mangani M. Darwish The Finite Volume Method in Computational Fluid Dynamics an Advanced Introduction with OpenFOAM® and Matlab, Springer 2016.

4.2 THE FINITE ELEMENT METHOD

The finite element method (FEM) is a numerical method which simplifies boundary value problems for partial differential equations in a system of algebraic equations, by yielding approximate values of the unknowns at discrete number of points over the domain. To solve the problem, it subdivides a large one into a smaller one, through simpler parts that are called finite elements. The simple equations, modelling these finite elements, are then assembled into a larger system of equations that simplify the entire problem. Afterwards FEM uses variational methods from the calculus of variations to approximate a solution by minimizing an associated error function. This technique shows various advantages:

- Accurate representation of complex geometry
- Inclusion of dissimilar material properties
- Easy representation of the total solution
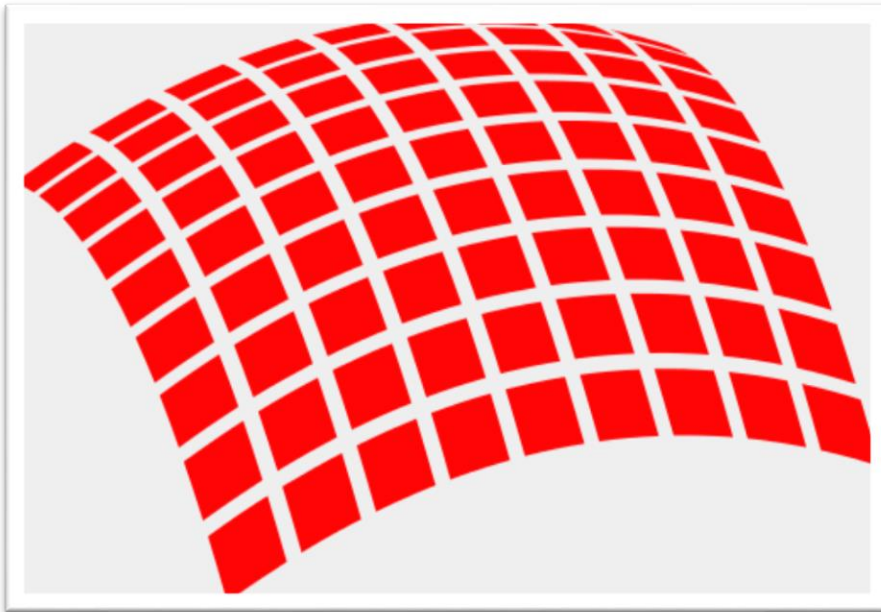- Capture of local effects.

Figure 4.2 Mesh discretization of a surface in a certain number of elements.

4.3 MULTIFRACTAL ANALYSIS

A fractal is a geometric object with internal homothety, which is a particular geometrical transformation of the plane or of the space, which dilates or contracts the objects, by keeping the corners unchanged, namely the form. A fractal repeats itself in its same form on different scales, and therefore by enlarging any part of it a figure similar to the original is obtained (figure 4.3.1); it is studied by the fractal geometry which belongs to non-Euclidean geometry.
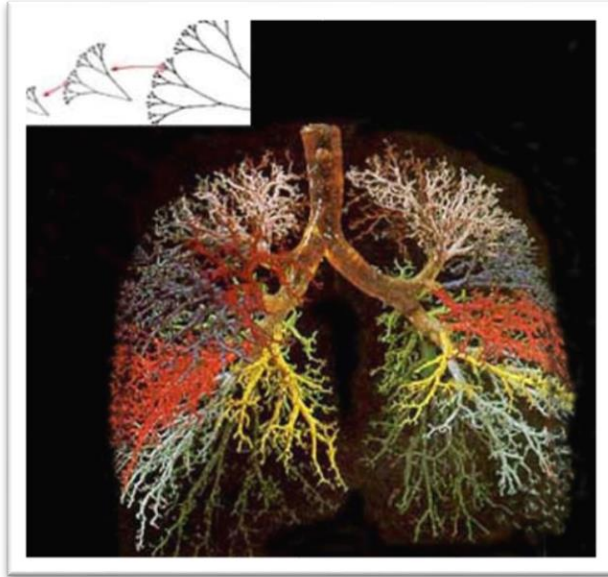

Figure 4.3.1 The branches in the lungs. They are an example of fractal in nature. Indeed, the structure of bronchi in space is based on the repetition of a single branch in various sizes like a tree.

A substantial difference between a geometric Euclidean object and a fractal is the way in which it is constructed. A flat curve is generally built on the Cartesian plane, using a function depending on t (time), such as in circular motion the equation of motion:

$$s(t) = R\omega(t)$$

Where ω is angular speed. On the contrary, fractals are developed as of an algorithm, which lets us draw curve and it is never applied only once, but the procedure is iterated a number of times theoretically infinite: at each iteration, the curve gets closer and closer to the final result by approximation. Fractals are distinguished in three groups:

- Linear fractals: the algorithm is linear, hence the terms are of first order.
- Non-linear fractals: the algorithm presents terms with order above first one.
- Random fractals (figure 4.3.2).

Hence, they have two main features:

- Self-resemblance: it is the union of copies of itself at different scales;
- Fine structure: the detail of the image does not change at every enlargement;

With respect to fractals dimension, namely Hausdorff–Besicovitch dimension (D_h), it determines fractals 'roughness' and it is a statistical quantity that gives an indication of how complete a fractal appears to fill the space.

$$D_h = -\frac{ln N_r}{ln\frac{1}{r}} \ (4.1)$$

Among the methods which are able to calculate fractal dimension, there is the box-counting method which was the first to solve (4.1), by evaluating N_r with a certain algorithm. The latter is based on some steps: a meshing of the binary signal, the formulation of a probability in each generated box and the estimation of the fractal dimension by a least-squares linear fitting as last step. So, by coating totally a binary signal with N(r) boxes of length r, the fractal dimension is given by:

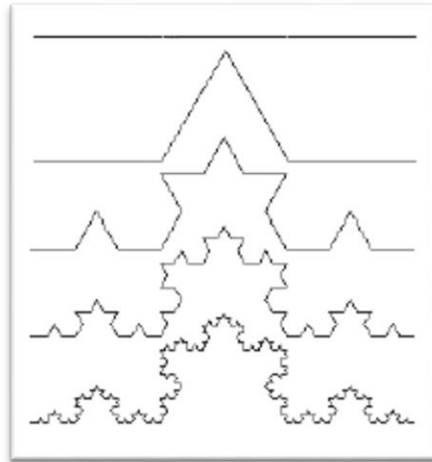$$D_B = \lim_{r \to 0} \frac{ln N(r)}{ln r} \ (4.2)$$

Figure 4.3.2 Kock's curve. It is a fractal curve which has the following characteristics: infinite perimeter, finite area, self-similarity, fractional size.

With regards to multifractal, it could be seen as an extension of fractal, however it is more complex in the sense that it is always invariant by translation, even if the dilatation factor requested to be able to distinguish the detail from the whole object depends on the detail being observed, as Lopes and Betrouni report [8]. Initially, Multifractal analysis was applied in fluid dynamics to determine the velocity in turbulent flow. In this case, a signal treatment approach has been developed because the velocity shows a complex structure. This procedure tries to define in each signal point x_0 the velocity variation law to determine the punctual Hölder exponent $h(x_0)$. All of points with the same exponent h are grouped into sets S_h, whose topological dimension is important in term of measure. Thereby, they searched to calculate the D_h of S_h and the function $h \to D_h$ was called the singularity spectrum. Due to this function was difficult to be determined by numerical computation, "the multifractal formalism" has been elaborated:

$$D(h) = \lim_{q \to \infty} (q \cdot h - \tau(q) + c)$$

Where q is the probability moment, it is a real number and allows to explore different regions of the singular measurement, c is a constant and $\tau(q)$ is called the partition function. By indicating with D_q the generalized dimensions of the multifractal spectrum, for q>1 it indicates the more singular regions, for q<1 it represents the less singular ones and for q=1 D_q indicates the information dimension. By the way, a multifractal structure can be seen as a superposition of homogeneous mono fractal structures. Indeed, for instance we can consider the mono fractal

structure E(h), which is a set of Hölder exponents h of particles with values in the interval [h, h+Δh], and F(h) which is the dimension of E(h). (q, τ(q)) and (h, F(h)) are linked by the Legendre transform:

$$\tau(q) = q \cdot h(q) - F(h)$$

$$h(q) \cong \alpha(q) = \frac{d\tau(q)}{dq}$$

Where α is an approximation of Hölder coefficient h and it is called singularity strength. Hence, for a multifractal structure the dimensions D_q are decreasing functions of q and h → F(h) is a convex function with maximum in D_h. So, in light of these considerations, the standard box-counting method for multifractal spectrum system is a generalization of a fractal system, where the signal is meshed with various boxes of size r and a normalized measure is computed in each box. This technique is used to analyse points sets, described by an infinite number of generalized dimensions D_q and by the multifractal spectrum function f(α). D_q is a function of q and f(α) is obtained by Legendre transform. Moreover, the algorithms are distinguished by low statistics, above all for q<0 [8]. This method along with the other box-counting techniques like the "sand box" and the wavelet leaders method are employed in clinical applications in order to obtain an image segmentation, such as for:

- electrocardiogram (ECG) and electroencephalogram (EEG) signals
- brain imaging
- mammography and bone imaging

In particular, in this dissertation, the standard box-counting method for multifractal spectrum has been used in CFD clinical application as reported in Chapter 6.

CHAPTER 5

CFD APPLIED IN THE RESPIRATORY SYSTEM

5.1 CARRYING OUT A CFD ANALYSIS IN THE RESPIRATORY SYSTEM

In this field of study, the effects of the mean flows are important and the drag force acting on the particle, if it is present, is also prominent to nasal flow simulations. In this last case the Lagrangian technique is preferred, indeed this method lets us follow numerically the single particle's movement caused by the forces applied and its interaction with various eddies in a turbulent flow. In the circumstance of turbulence fluctuations the Reynolds-averaged Navier-Stokes (RANS) equations are employed, in fact they assess the effects of turbulence on the mean flow field over averaged time. Besides the simulations using RANS on modelling turbulent flows should be associated with an eddy interaction model or random walk model. The latter is a stochastic process and describes a path that consists of a succession of random steps on some mathematical space. Although the nostrils assume in their cavities a laminar condition which can be encountered in the adults during the resting breathing, as Garcia [9] stresses, the analysis is enforced under a turbulent one and more thoroughly it has been pointed out by Liu [10] that the turbulence kinetic energy characterizes the first half part of the domain and then it decreases to zero in a certain zone beyond the nostrils. Clearly it is necessary to fix the domain of interest, the boundary conditions and indicate the time-dependence or independence.

5.2 THE DOMAIN

The determination of the domain depends much on the geometry and grid generation, by the way there are strong differences in the airflow distributions caused by the various structures of the nasal cavities among people as Yu [11] underlines. In order to develop an accurate simulation of the airflow which travels the airways, it is needed to scan the whole nose from the nasal tip to the posterior wall of nasopharynx by using the Computerized (Axial) Tomography and the Magnetic Resonance (Imaging) to build a precise geometric model of the nasal cavities. Indeed, it is necessary to consider the influence of the nostrils in the aspiration of the air and the limitation of the nasopharynx in directing the airflow towards the pharynx, as Bailie [12] points out. Since the computational and time costs increase with the reduction of the dimensions of the control volumes, it is prominent the attention to the dimensions of the grids. Therefore, in CFD, the unstructured grids are a tessellation of a part of the Euclidean plane or Euclidean space by simple shapes, such as triangles or tetrahedra, in an irregular pattern. They ensure, by contrast, to the structured grids having a repeating structure, more flexibility and the possibility to build complex geometries like the nose.

5.3 BOUNDARY CONDITIONS

The boundary conditions (BCs) are of importance in the representation of the phenomena. Some researchers prefer to the define outlet BCs than the inlet ones, because they are able to point out better the physiologic conditions of drawing the air throughout the nasopharynx. However, the inlet BCs are worthwhile with respect to the drug delivery methods, because the air is pushed into the nostrils by, for instance, a device which releases the drug particles with momentum and, for this reason, these conditions are able to simulate precisely the deposition of the drug. In the problems of deposition there is another aggravation represented by the mucus which delays the laying of the drug on the nasal cavity walls.

5.4 TIME DEPENDENCY

Even if the respiration nasal airflow is considered like a steady flow, transient simulations are required when the phenomena change during the investigation. They take much more time due to the reaching of the convergence at each step and they have let expand the applications of CFD [13].

CHAPTER 6

THE CFD-FRACTAL METHOD APPLIED IN DETECTING A GROWING BRONCHIAL TUMOUR.

After the description of the CFD math methods being discussed on this dissertation, in this chapter a recent application of the CFD-multifractal technique, based on Xi and Jon Kim's sample published in 2015 [14], is presented. This study deserves to be reported, because a non-invasive breath test for the detecting of tumours has been elaborated thanks to CFD, thereby we can understand that CFD can be very worthwhile in medical field too. Furthermore, this possible and future test will be able to let people avoid invasive exams, such as the biopsy, and it will be able to speed up the examination's time so that it can be helpful for people who suffer from tumours. Naturally, this potential clinical exam has to be still studied and tested on human patients, indeed, so far, the experimentations have been applied only on animals, like rats, and on computer, thanks to 3D simulations, nevertheless its employment appears to be economic, non-invasive, immediate in response and easy to use.

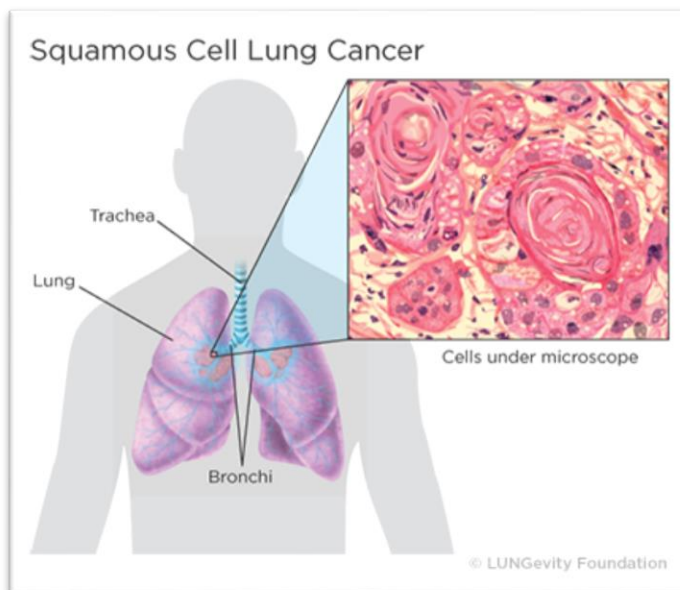## 6.1 THE TEST AND THE BRONCHIAL TUMOUR

Figure 6.1 A squamous cell lung cancer.

This clinical exam concerns the study of the inhaled and exhaled aerosols distribution which is produced in lungs throughout a bolus of tracer particles being inhaled first and then exhaled. Aerosols patterns are altered by a growing bronchial tumour (figure 6.1), and thanks to these variations it is possible to detect the disease presence and site, determine its severity and formulate a targeted drug delivery plan to treat the disease. The basis of this test is the conviction that each lung has got its aerosol fingerprint (AFP) in contrast to fingerprints of VOCs (volatile organic compounds) breath tests which measure without localizing them. Thereby, a deviation from the AFP pattern of healthy lungs would suggest an airway remodelling or tumorigenesis in the tested lungs, besides it was proved that multifractal analysis could effectively be applied

to distinguish the AFP patterns of diseased lung from healthy models, in fact it is able to identify the heterogeneity and complexity spaces filled by particles in lungs.

6.2 METHOD

The reported model is based on the sample present in [14], according to which the mouth at the top of the airway has got a diameter by 21 mm and the bronchi branches are until the sixth generation. The prototype has been based on a heathy adult male trachea which, afterwards, has been modified on computer in order to develop a squamous bronchial tumour in five different stages (figure 6.2). The latter, which grows as of round cells that replace the damaged cells on lung epithelium, is situated in the left segmental branch.

Size and severity of squamous tumor

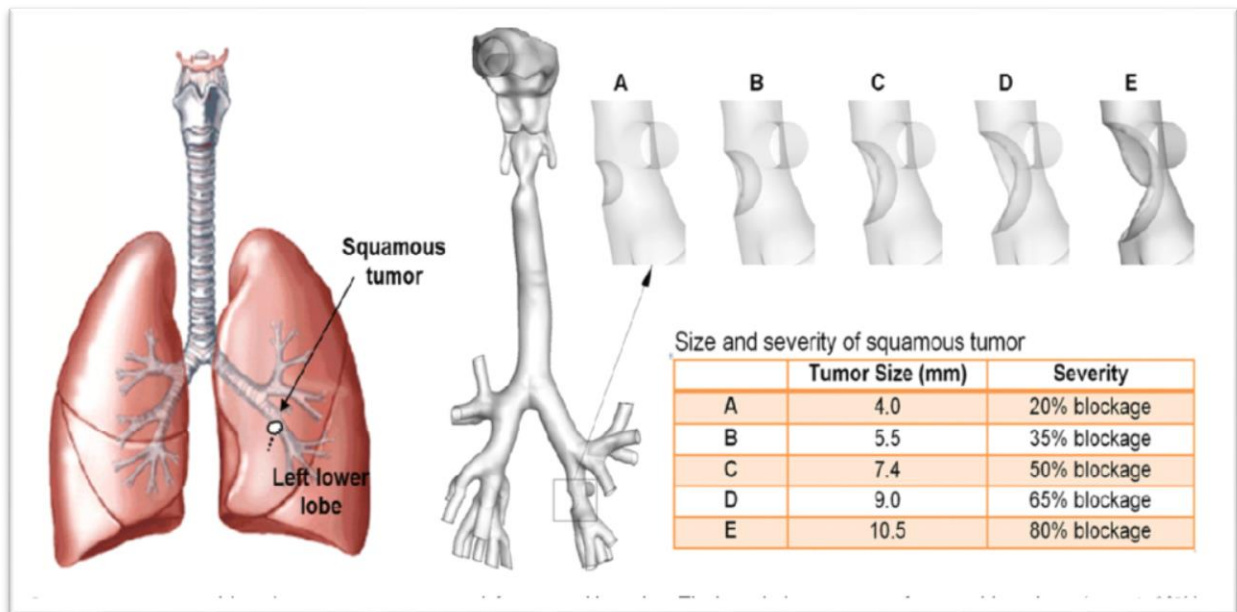|	Tumor Size (mm)	Severity
A	4.0	20% blockage
B	5.5	35% blockage
C	7.4	50% blockage
D	9.0	65% blockage
E	10.5	80% blockage

Figure 6.2 The location and various dimensions of the squamous tumour. Figure taken from Xi Jinxiang, Kim JongWon, Si Xiuhua A., Corley Richard A., Kabilan Senthil, Wang Shengyu, 2015, CFD Modeling and Image Analysis of Exhaled Aerosols due to a Growing Bronchial Tumour: towards Non-Invasive Diagnosis and Treatment of Respiratory Obstructive Diseases, Theranostics, 5, Issue 5.

First of all there is the image acquisition by simulation and eventually there is the fractal and statistical analysis, in order to obtain the exhaled aerosol pattern. A bolus of tracer particles is inhaled and exhaled to simulate inhalation and exhalation. These particles have the same initial velocity profile of the airflow and they are recorded on the surface of the bronchial exit, afterwards with respect to the exhalation, the particles flow is reversed in direction along with their profiles and they are deposed on a filter at the mouth of the airway. When the images have been collected, the mathematical part begins, indeed the results are analysed in terms of particle concentration distribution, relative concentration to the control case and in terms of location distribution. Afterwards, the resulting images are quantified by using statistical distribution in translational, radial, and circumferential directions (6.1) to describe the spatial pattern of the

AFPs, regional and localized fractal analysis (4.1), and multifractal analysis (4.2). In turn, the results can be used to evaluate the stage of tumour growth.

6.3 MATHEMATICAL MODELS TAKEN FROM CFD

With respect to the CFD models, the airflows have been considered as isothermal, incompressible and steady in time, in addition large eddy simulation approach has been adopted since it allows to pass from laminar regime to turbulent one and the Lagrangian description has been employed to track the particles of a diameter d_p:

$$\frac{dv_i}{dt} = \frac{f}{\tau_p C_c}(u_i - v_i) + g_i(1 - \alpha) + f_{i,Brownian} + f_{i,Lift} \quad (6.1)$$

where u_i is the fluid velocity, and v_i is the particle velocity. The particle residence time τ_p is defined as:

$$\tau_p = \rho_p \frac{d_p{}^2}{18\mu}$$

then f is the friction coefficient (seen in the paragraph 3.3) and C_c is the Cunningham correction factor which is used to account for non-continuum effects when the drag on small particles is calculated. Cunningham correction factor is remarkable for particles of order of 15 μm with air at ambient conditions.

$$C_c = 1 + \frac{2\lambda}{d_p} \cdot \left(A_1 + A_2 \cdot e^{\frac{-A_3 \cdot d_p}{\lambda}} \right)$$

Where λ is the mean free path and A_n are experimentally determined coefficients that for air are: $A_1 = 1.257$, $A_2 = 0.400$, $A_3 = 0.55$.

6.4 FRACTAL AND STATISTICAL ANALYSIS

The Box-counting method (D_B) for the multifractal analysis, which has been reported previously in the paragraph 4.3, has been used as mathematical base in this survey. This method is a measure of increasing details with decreasing resolution scales and it is calculated as the slope of the log-log plot between the box size (or scale, ε) and box count N_ε, which is the number of grid boxes containing pixels:

$$D_B = \lim_{\varepsilon \to 0} \frac{lnN(\varepsilon)}{ln\varepsilon}$$

The multifractal analysis benefits from the scaling properties of natural systems; in order to determine the multifractal dimensions, a normalized number $\mu_i(q,\varepsilon)$ has been elaborated with a family of scaling exponents q, used as distorting elements to explore various regions of a single measure.

$$\mu_i(q,\varepsilon) = \frac{[P_i(\varepsilon)]^q}{\sum[P_i(\varepsilon)]^q}$$

where $P_i(\varepsilon)$ is the probability of pixels at the ith box of size ε:

$$P_i(\varepsilon) = \frac{m_i(\varepsilon)}{M(\varepsilon)}$$

Where $m_i(\varepsilon)$ is the number of pixels or mass in any box i^{th} of size ε and $M(\varepsilon)$ the total mass or sum of pixels in all boxes for this ε.

$$M(\varepsilon) = \sum_{i=1}^{N_\varepsilon} m_i(\varepsilon)$$

Accordingly, the singularity strength $\alpha(q)$ and multifractal spectrum function $f(\alpha_q)$ with respect to $\mu i(q,\varepsilon)$ are given by:

$$\alpha(q) = \lim_{\varepsilon \to 0} \frac{\sum \mu_i(q,\varepsilon)\ln P_i(\varepsilon)}{\ln(\varepsilon)}$$

$$f(\alpha_q) = \lim_{\varepsilon \to 0} \frac{\sum \mu_i(q,\varepsilon)\ln\mu_i(q,\varepsilon)}{\ln(\varepsilon)}$$

The plot between $\alpha(q)$ and $f(\alpha_q)$ gives the multifractal spectrum image. In addition the data provided by the exhaled aerosols have been then undertaken throughout standard deviation for each of five breath test and the analysis of variance.

6.5 ANALYSIS OF AIRFLOW FIELD

From figure 6.5 (a) and (b), it is clear that the distortion of streamlines increases with the growth of obstruction represented by the disease site, such alteration is also notable in the cross-sectional velocity contours. Besides, there is a higher and higher flow resistance from case A to case E caused by the decrease of dimensions of airflow area due to the growth of the tumour, accordingly there is a lower and lower respiratory flow rate under the same breathing effort. In addition, the airway obstruction alters the pattern of exhaled aerosol. Concerning the velocity profiles represented in figure 6.5 (c), it is fair that they diminish as the tumour increases in size, moreover they decrease as long as the distances grow and they go downstream. Even if downstream airflows might appear similar, the particle profiles could still be different due to their time-integrative properties.
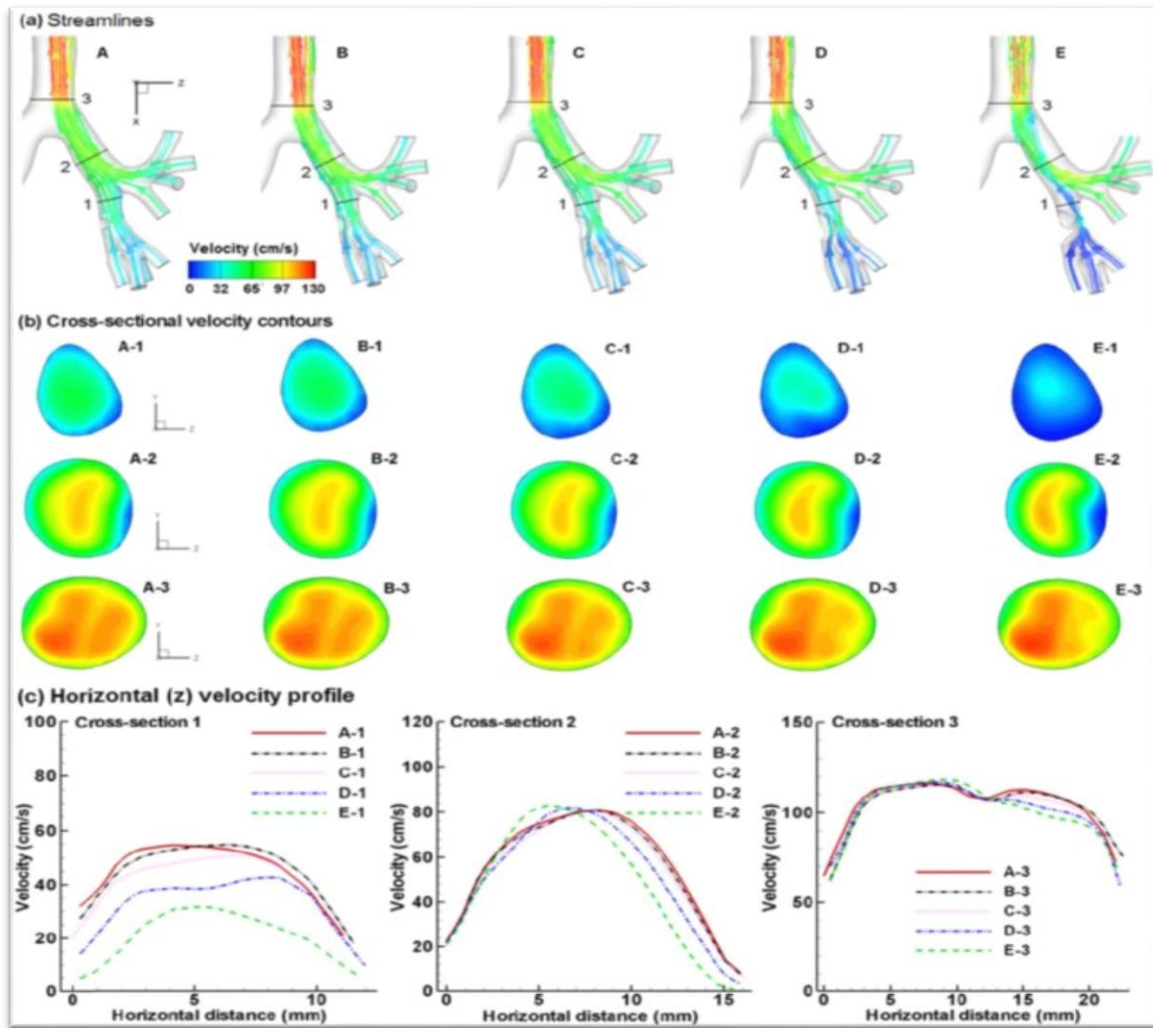
Figure 6.5 The differences in expiratory flow among five stages of the evolution of the tumour with respect to the deviation of the streamlines, the cross-sectional velocity contours and the velocity profiles. Figure taken from Xi Jinxiang, Kim JongWon, Si Xiuhua A., Corley Richard A., Kabilan Senthil, Wang Shengyu, 2015, CFD Modeling and Image Analysis of Exhaled Aerosols due to a Growing Bronchial Tumour: towards Non-Invasive Diagnosis and Treatment of Respiratory Obstructive Diseases, Theranostics, 5, Issue 5.

6.6 PATTERNS OF EXHALED AEROSOL FINGERPRINTS

Figure 6.6 (a) and (b) show the location and concentration distributions, in particular from the first row we can see a vortex of exhaled particles in the left-hand corner which remains steady in all of five cases, by contrast in the regions highlighted by the red dashed box and circle the amount of particles decreases progressively, indeed there is an evident dispersion from A to E. These results are reflected also in the second row, using red for high concentration and blue for low concentration, hence we can see that in the same zones, previously pointed out by the red box and circle, there is major presence of blue as moving from A to E. This dissimilarity in concentration stresses the growth of the tumour. The last right of figure 6.6 shows the relative comparison by subtracting the concentration of cases B-E (tested cases) from that of A (control case) and in doing these operations the red colour for the peak concentration of tested case and blue one for that of the control case are used. Thanks to this comparison, if there is the same distribution of particles but with opposite colours in two adjacent spots, like for instance in the black dotted circle in the third row, we can note the migration of the particles between the spots caused by the various stages of tumour, accordingly this evidence may be used to detect the latter and monitor its growth.
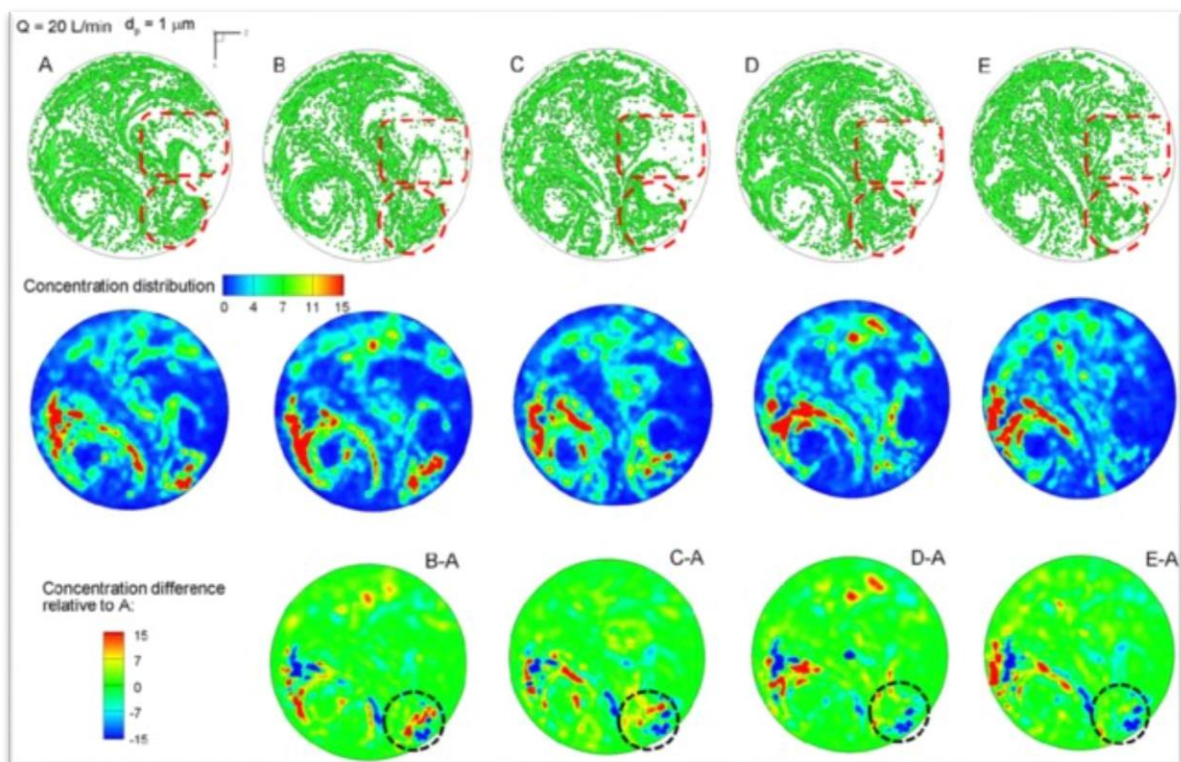

Figure 6.6 Particle distributions collected at the mouth for an aerosol size of 1 μm and a flow rate of 20 L/minute. Figure taken from Xi Jinxiang, Kim JongWon, Si Xiuhua A., Corley Richard A., Kabilan Senthil, Wang Shengyu, 2015, CFD Modelling and Image Analysis of Exhaled Aerosols due to a Growing Bronchial Tumour: towards Non-Invasive Diagnosis and Treatment of Respiratory Obstructive Diseases, Theranostics, 5, Issue 5.

6.7 DISCUSSION OF RESULTS

Hence, the methodology, adopted in [14], presents two steps: individuation of the lung tumour and its localization. The first AFP, acquired at different time, can be compared and thanks to their comparison the eventual disease can be highlighted, in fact from the differences we can figure out the stage of the tumour, while from the similarities its position. Whenever there was a tumour, the next step would be using detective aerosols, namely chemical-sensitive aerosols which are able to change the colour when they meet VOCs of the disease. If much particles of aerosols change colour, thereby the site of the tumour is correct, as example of a right individuation of the disease there is figure 6.7 which shows the inhaled particles deposited on tumour and the patterns of those exhaled. By increasing the airway obstruction, the number of exhaled particles decreases sharply, indeed in case E we can note the lowest amount of particles. Moreover, from the example proposed in [14] (Figure 6.7 (c)), particles deposit mostly on the diagonal zone of the blue ellipse in each case, this common sign can be regarded as a signature of the lower-left lobe region and it can be utilised to pinpoint more accurately the disease and deliver drugs against it.
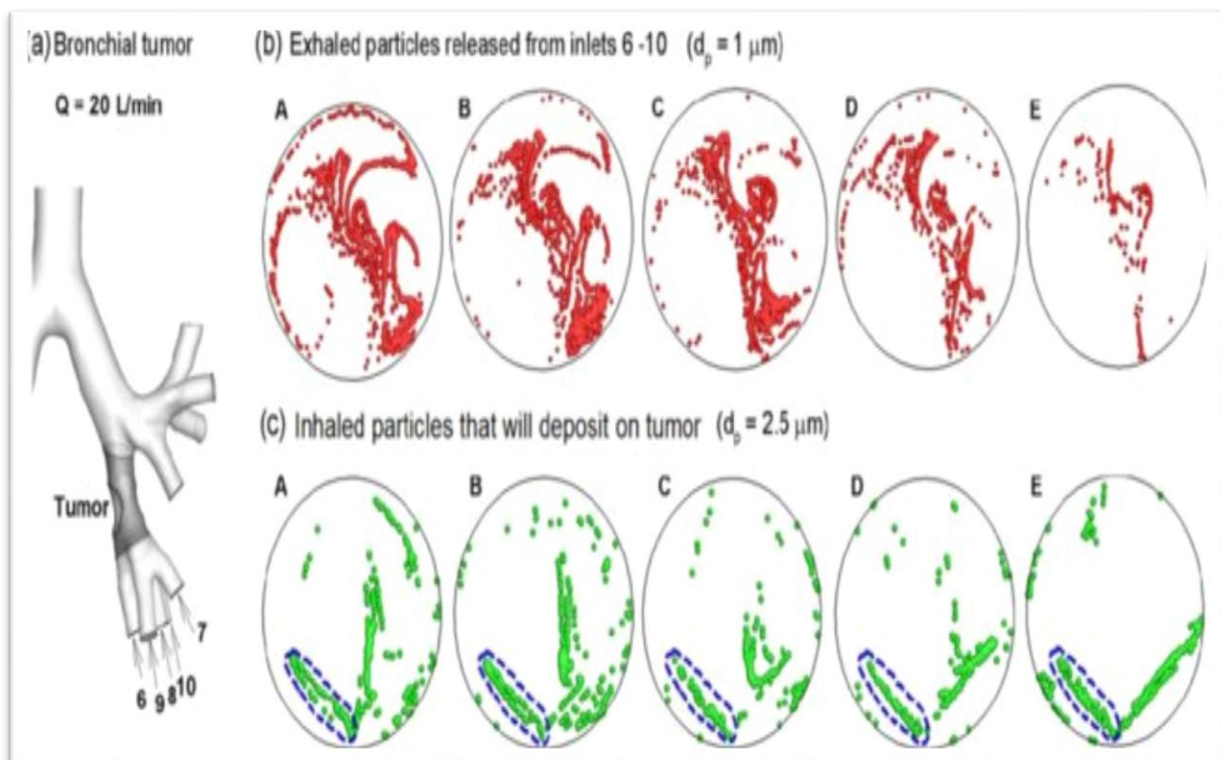

Figure 6.7 (a) The site of the tumour, while in (b) and (c) there are the patterns of exhaled and inhaled particles but with different diameter. Figure taken from Xi Jinxiang, Kim JongWon, Si Xiuhua A., Corley Richard A., Kabilan Senthil, Wang Shengyu, 2015, CFD Modelling and Image Analysis of Exhaled Aerosols due to a Growing Bronchial Tumour: towards Non-Invasive Diagnosis and Treatment of Respiratory Obstructive Diseases, Theranostics, 5, Issue 5.

The goal would be obtaining a theranostic (therapeutic-diagnostic) device which would be able to detect the lung disease and provide a cure. Anyway, Xi and Jon Kim have demonstrated the feasibility of CFD-fractal analysis to detect eventual lung tumours thanks to the study of the aerosol fingerprints of the lungs, indeed AFPs allow to pinpoint the presence of a disease, monitor its evolution in time, or track the therapeutic outcomes of an intervention protocol. This non-invasive breath test might be employed to control those people who are more subject to develop lung diseases, in this way we could increase the probability to kill the tumour since we would have detected it long before.

CHAPTER 7

OPTINOSE

In this chapter another recent application of CFD is reported, in this case the computational fluid dynamics has allowed to optimise a drug releasing device to the nasal mucous membrane, developed by the Norwegian branch of the American company OPTINOSE®. The pioneering aspect does not only stay in the device in its self, but also in the bidirectional release system which has been elaborated thanks to CFD, as reported in [15]. This device based on this delivery method seems to be the most efficient, as indicated by M. Obaidi and E. Offman [16]. Moreover, CFD has been able to reduce the time and costs of laboratory experiments in the development of this instrument.

7.1 MATHEMATICAL ELABORATION

Firstly, it has been needed to build a proper surface grid of the nasal cavity, secondly the latter has been inserted into Tgrid which produces a volume grid thanks to the finite volume method (4.1). Naturally, the cell quality has been tested during the surface grid and volume grid generation and finally the obtained patterns have been inserted in the commercial CFD code FLUENT.

7.2 FUNCTIONING

This device (figure 7.2) is constituted by a mouthpiece and a shaped sealing nosepiece that has been designed to benefit from nasal anatomy and physiology to improve the spread of drug delivery meantime protecting against the risk of lung inhalation, furthermore it utilizes the force impressed by the patient and the pression generated during the oral exhalation in the oropharynx to release the drug. In fact, first of all this positive pressure lets the soft palate go up and keep it close in order to separate nasal and oral cavities (figure 2.4.1), secondly this pressure, which has been reduced, is transferred into nasal cavity where it balances the one that acts across the soft palate in order to preserve the communication between the nostrils. Indeed, after the drug, mashed with exhaled air (aerosol), has spread from one nostril to the deep nasal cavity, the aerosol escapes by the other nostril: this mechanism is called bidirectional delivery ad it is explained visually on the OPTINOSE web page [17].

Figure 7.2 OPTINOSE® device. We can see the mouthpiece, which is the part sidelong, and the nosepiece, that is at the top of the device. Figure taken from https://www.optinose.com/.

7.3 RESULTS

The performance of the device (BREATH POWERED DEVICE) developed by OPTINOSE[®] has been discussed in [16]. They have tested the same antimigraine drug, Sumatriptan, in four different ways of administration on a group of 20 healthy people. Sumatriptan has been administrated orally by tablet, by subcutaneous injection and by intranasal way throughout the OPTINOSE device and traditional spray device. With respect to the tablet and subcutaneous injection, although the first one is the most used method, it can lead to some gastroinstestinal problems in the patients, while the second one determines a high percentage of side effects. By contrast, the traditional spray device is less efficient, in fact one part of the dose of the drug stops in the part of the nasal cavity anterior to the narrow nasal valve located about 2 cm into the nose (figure 2.4.2), where there are not ciliated surfaces, thereby the absorption is highly reduced, besides a large fraction of the remaining drug does not deposit into the deep nasal cavity as the standard aerosol does, but it is drawn into the pharynx and swallowed (figure 7.3 (a)).
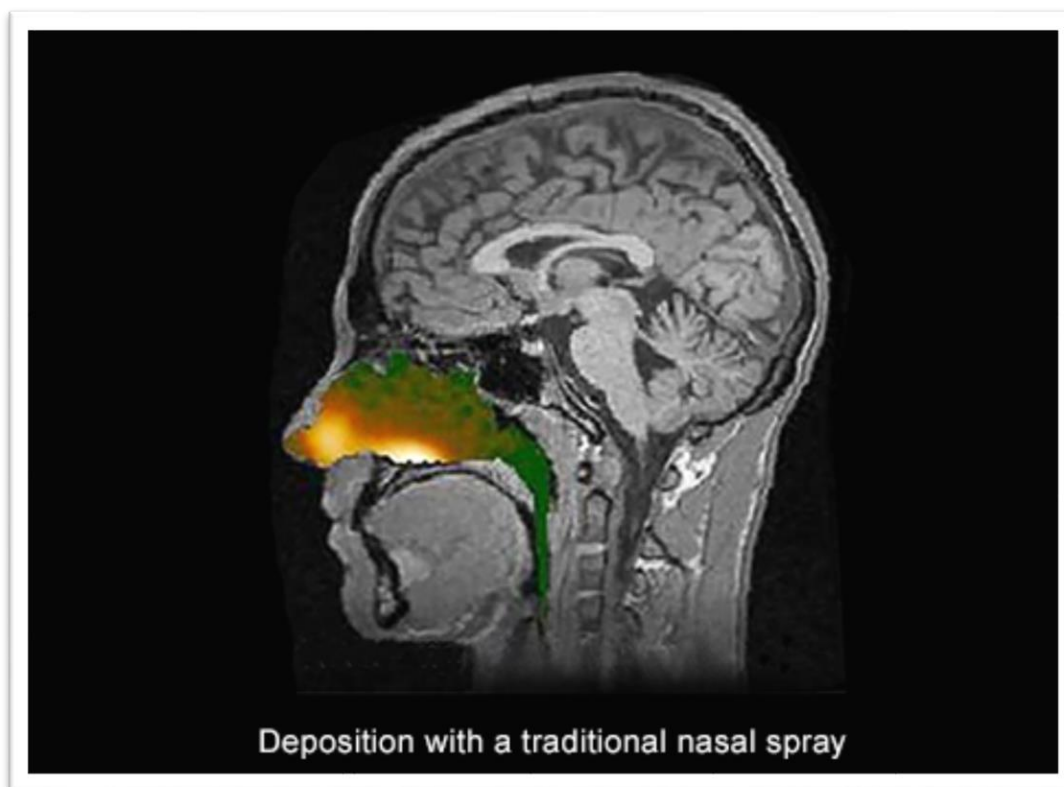
Figure 7.3 (a) Deposition with a traditional nasal spray. We can note the reduced distribution of the drug (in orange colour) into the nasal cavities. Figure taken from Obaidi Mohammad, PhD; Offman Elliot, BSc, Pharm MSc; Messina John, PharmD; Carothers Jennifer, ScD; Djupesland Per G., MD, PhD; Mahmoud Ramy A., MD, MPH, 2013, Improved Pharmacokinetics of Sumatriptan With Breath Powered™ Nasal Delivery of Sumatriptan Powder, Wiley Periodicals.

As opposed to the traditional delivery system and the other methods of administration, OPTINOSE assures a major and faster absorption even with small doses thanks to its superior delivery pattern to the deep nasal zones beyond the nasal valve (figure 7.3 (b)), in addition it produces a significant lower peak and total systemic exposure than oral tablet or subcutaneous injection.
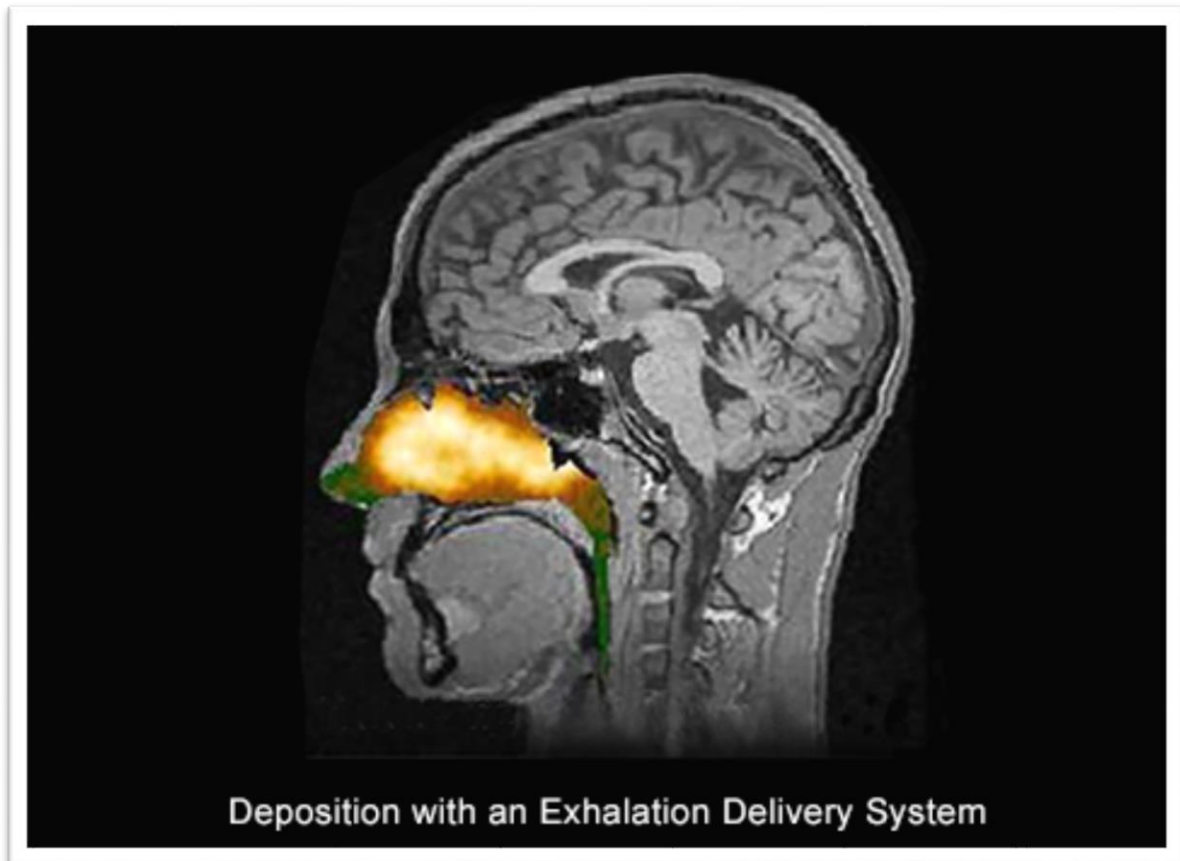
Figure 7.3 (b) Deposition with an exhalation delivery system. It is noticeable the major deposition of the drug, which is not swallowed. Figure taken from Obaidi Mohammad, PhD; Offman Elliot, BSc, Pharm MSc; Messina John, PharmD; Carothers Jennifer, ScD; Djupesland Per G., MD, PhD; Mahmoud Ramy A., MD, MPH, 2013, Improved Pharmacokinetics of Sumatriptan With Breath Powered™ Nasal Delivery of Sumatriptan Powder, Wiley Periodicals.

CHAPTER 8

CONCLUSIONS

From the reading of this dissertation it is noticeable that CFD applications in human biology help to comprehend better the functioning of that complex machine which we call human body, indeed Thomas Young said [18]:

"The mechanical motions, which take place in animal body, are regulated by the same general laws as the motion of inanimate bodies [. .] and it is obvious that the enquiry, in what matter and in what degree, the circulation of the blood depends on the muscular and elastic powers of the heart and of the arteries [. .] must become simply a question belonging to the most refined departments of the theory of hydraulics."

While physical experiments in vitro and in vivo are usually expensive and time-consuming, CFD turns out to be faster and it can be very worthwhile provided the operator is experienced, indeed computational fluid dynamics allows to reproduce certain phenomena which are hardly performed in laboratory. However, in order to ensure the precision and trustworthiness of CFD simulations, predictions need to be proved against reliable measurements achieved in parametric studies. CFD has been allowing also to develop new medical devices either as drug releasers, such as OPTINOSE drug releasing device, and as techniques to monitor human health, like the tumour detecting breath test reported in chapter 6.

Undoubtedly, the potential breath tumour-test shows some advantages, for instance it can be helpful to detect some lung diseases more rapidly, less invasively and without damaging our health than the traditional PET and tissue biopsy, which, however, will not be able to be replaced totally. Indeed, the latter could be required for a microscopic analysis of the cancer cells in order to confirm the mathematical data. Besides, this breath test could allow people to save time, in fact the public hospitals are too crowded with regards to the medical analysis, and it could be an optimum instrument in those cases in which the biopsy turns out to be difficult and too invasive towards the patient or the latter is COPD or asthmatic, hence the airways are more closed. By the way, the question of the breath test is still opened, because it requires further experimentations, in particular about the acceptance of possible breathing deviations caused by compliant walls; the detection sensitivity, influenced by hygroscopic growth and dynamic glottis and the correct manoeuvres in order to optimize the breath test.

What respect to OPTINOSE drug releasing device, it is certainly an optimum tool of delivery drug for migraine headache, indeed it produces a faster and more efficient absorption profile than the traditional drug dosing devices, although the administering is to a single nostril. However, it is needed further research to delineate well the potential clinical benefits of this releasing drug form, in particular on the women, because the survey in [16] has interested above all men. Moreover, it is required a more precise experimental measure of the drug absorbed throughout the nasal mucosa.

REFERENCES

[1] Sir Lighthill J., 1975, *Mathematical Biofluiddynamics*, chap. I, XI. University of Cambridge.

[2] Ambrosi G., Cantino D., Castano P., Correr S., D'Este L., Donato R. F., Familiari G., Fornai F., Gulisano M., Iannello A., Magaudda L., Marcello M. F., Martelli A. M., Pacini P., Rende M., Rossi P., Sforza C., Tacchetti C., Toni R., Zummo G., 2006, *Anatomia dell'uomo seconda edizione*, chap.9. Edi. Ermes.

[3] Mazzoldi P., Nigro M., Voci C., 2014, *Fisica Volume I*, chap.8. Edises.

[4] Arina R., 2015, *Fondamenti di Aerodinamica*, chap.2. Levrotto & Bella.

[5] Chioccia G., Germano M., 2007, *Termofluidodinamica*, 2.ed. chap.6. Levrotto & Bella.

[6] Caro C.G., Pedley T.J., Schroter R.C., Seed W.A., 1978, *The Mechanics of the Circulation*, part 1, chap.5. Oxford University Press.

[7] Pedley T. J., Schroter R. C., Sudlow M. F., 1970, *Respiration physiology*, 9, 371-405.

[8] Lopes R., Betrouni N., 2009, *Fractal and multifractal analysis: A review*, Medical Image Analysis 13, 634-649.

[9] Garcia G. J. M., Bailie N., Martins D. A, Kimbell J. S, 2007, *Atrophic rhinitis: A CFD study of air conditioning in the nasal cavity*, J Apply Physiology 103:1082-1092.

[10] Liu Y., Matida E. A., Gu J., Johnson M. R*., 2007, *Numerical simulation of aerosol deposition in a 3-D human nasal cavity using RANS, RANS/EIM, and LES*, J Aerosol Sci 38:683-700.

[11] Yu S., Liu Y., Sun X., Li S., 2008, *Influence of nasal structure on the distribution of airflow in nasal cavity*, Rhinology 46.

[12] Bailie N., Modelling nasal airflows, 2005, Ph.D. Thesis, Queen's University of Belfast.

[13] Kleven M., Melaaen M. C., 2012, *Computational fluid Dynamics (CFD) applied in the drug delivery design process to the nasal passages: a review*, Journal of Mechanics in Medicine and Biology, World Scientific Publishing Company©. Vol. 12, No. 1 1230002 (17 pages). DOI: 10.1142/S0219519411004526.

[14] Xi Jinxiang, Kim JongWon, Si Xiuhua A., Corley Richard A., Kabilan Senthil, Wang Shengyu, 2015*, CFD Modeling and Image Analysis of Exhaled Aerosols due to a Growing Bronchial Tumor: towards Non-Invasive Diagnosis and Treatment of Respiratory Obstructive Diseases*, Theranostics 2015, vol.5, Issue 5, pp.443-455. DOI: 10.7150/thno.11107.

[15] Kleven M., Melaaen M., Reimers M., Rotnes J. S., Aurdal L., Djupesland P. G., 2007, *Using computational fluid dynamics (CFD) to improve the bi-directional nasal drug delivery concept*, Trans IChemE, Part C, Food and Bioproducts Processing., 83(C2): 107-117.

[16] Obaidi Mohammad, PhD; Offman Elliot, BSc, Pharm MSc; Messina John, PharmD; Carothers Jennifer, ScD; Djupesland Per G., MD, PhD; Mahmoud Ramy A., MD, MPH, 2013, *Improved Pharmacokinetics of Sumatriptan With Breath Powered™ Nasal Delivery of Sumatriptan Powder*, Wiley Periodicals, pp.1-3. DOI: 10.1111/head.12167.

[17] OPTINOSE® incorporated, 2018, "Exhalation Delivery Systems", https://www.optinose.com/exhalation-delivery-systems/technical-overview.

[18] Young T., 1808, *The Croonian Lecture. On the functions of the heart and arteries*, DOI: 10.1098/rspl.1800.0173.